Hazard Assessment of Abraded Thermoplastic Composites Reinforced with Reduced Graphene Oxide

Document Version
Accepted author manuscript

OPEN ACCESS

Graphical abstract

Highlights

- Graphene related materials are mostly used to reinforce polymers
- Abrasion of composites materials is an important end-of-life scenario to be assessed prior large use
- This study provide a qualitative and quantitative analysis of the released materials after abrasion
- The hazard of the abraded thermoplastic is assessed focusing on the most likely exposure routes
- Life cycle consideration and impact of reduced graphene oxide in the context of reinforced polymers is addressed

Hazard Assessment of Abraded Thermoplastic Composites Reinforced with Reduced Graphene Oxide

Savvina Chortarea[1], Ogul Can Kuru[1], Woranan Netkueakul[1], Marco Pelin[2], Sandeep Keshavan[3], Zhengmei Song[4], Baojin Ma[4], Julio Gómes[5], Elvira Villaro Abalos[6], Luis Augusto Visani de Luna[7,8,9], Thomas Loret[7,8,9], Alexander Fordham[7,8,9] Matthew Drummond[7,8], Nikolaos Kontis[10], George Anagnostopoulos[10], George Paterakis[10], Pietro Cataldi[8,12], Aurelia Tubaro[2], Costas Galiotis[10,11], Ian Kinloch[8,12], Bengt Fadeel[3], Cyrill Bussy[7,8,9], Kostas Kostarelos[7,8,13], Tina Buerki-Thurnherr[1], Maurizio Prato[14,15,16], Alberto Bianco[4] and, Peter Wick[1*]

[1]Swiss Federal Laboratories for Materials Science and Technology (EMPA), Laboratory for Particles-Biology Interactions, 9014 St. Gallen, Switzerland.
[2]Department of Life Sciences, University of Trieste, 34127 Trieste, Italy.
[3]Nanosafety & Nanomedicine Laboratory, Institute of Environmental Medicine, Karolinska Institutet, 177 77 Stockholm, Sweden.
[4] CNRS, Immunology, Immunopathology and Therapeutic Chemistry, UPR3572, University of Strasbourg, ISIS, 67000 Strasbourg, France.
[5] Avanzare Innovacion Tecnologica S.L. 26370, Navarrete, Spain.
[6] Instituto de Tecnologías Químicas de La Rioja (InterQuímica), 26370, Navarrete, Spain.
[7] Nanomedicine Lab, Faculty of Biology, Medicine & Health, University of Manchester, Manchester M13 9PT, United Kingdom.
[8] National Graphene Institute, University of Manchester, Manchester M13 9PL, United Kingdom.
[9]Lydia Becker Institute of Immunology and Inflammation, Faculty of Biology, Medicine and Health, University of Manchester, Manchester Academic Health Science Centre, Manchester, M13 9PL, United Kingdom.
[10]Institute of Chemical Engineering Sciences, Foundation of Research and Technology-Hellas (FORTH/ICE-HT), 26504 Patras, Greece.
[11]Department of Chemical Engineering, University of Patras, 26504 Patras, Greece
[12]Department of Materials, University of Manchester, Manchester M13 9PL, United Kingdom
[13]Catalan Institute of Nanoscience and Nanotechnology (ICN2), and Barcelona Institute of Science and Technology (BIST), Barcelona 08193, Spain.
[14] Department of Chemical and Pharmaceutical Sciences, University of Trieste, 34127 Trieste, Italy.
[15]Center for Cooperative Research in Biomaterials (CIC biomaGUNE), Basque Research and Technology Alliance (BRTA), 20014 Donostia San Sebastián, Spain.
[16]Basque Foundation for Science (IKERBASQUE), 48013 Bilbao, Spain.

*Corresponding authors:

Peter Wick
peter.wick@empa.ch

Empa, Swiss Laboratories for Materials Science and Technology
Lerchenfeldstrasse 5
CH-9014 St. Gallen

Abstract

Graphene-related materials (GRMs) are subject to intensive investigations and considerable progress has been made in recent years in terms of safety assessment. However, limited information is available concerning the hazard potential of GRM-containing products such as graphene-reinforced composites. In the present study, we conducted a comprehensive investigation of the potential biological effects of particles released through an abrasion process from reduced graphene oxide (rGO)-reinforced composites of polyamide 6 (PA6), a widely used engineered thermoplastic polymer, in comparison to as-produced rGO. First, a panel of well-established *in vitro* models, representative of the immune system and possible target organs such as the lungs, the gut, and the skin, was applied. Limited responses to PA6-rGO exposure were found in the different *in vitro* models. Only as-produced rGO induced substantial adverse effects, in particular in macrophages. Since inhalation of airborne materials is a key occupational concern, we then sought to test whether the *in vitro* responses noted for these materials would translate into adverse effects *in vivo*. To this end, the response at 1, 7 and 28 days after a single pulmonary exposure was evaluated in mice. In agreement with the *in vitro* data, PA6-rGO induced a modest and transient pulmonary inflammation, resolved by day 28. In contrast, rGO induced a longer-lasting, albeit moderate inflammation that did not lead to tissue remodeling within 28 days. Taken together, the present study suggests a negligible impact on human health under acute exposure conditions of GRM fillers such as rGO when released from composites at doses expected at the workplace.

77 Graphene and its derivatives (graphene-related materials or GRMs) have been among the fastest
78 growing areas of nanoscience and technology over the past decade. This atomically thin, two-
79 dimensional form of carbon has generated considerable excitement since its initial discovery. Due
80 to its outstanding physicochemical properties, namely, excellent stretchability (20% of its initial
81 length), high intrinsic mechanical stiffness and strength (1 TPa and 130 GPa, respectively),
82 extraordinary electrical conductivity (mobility of charge carriers 200,000 $cm^2/$ V/s), large surface
83 area (2630 m^2/g), and superior thermal conductivity (~5000 W/mK), it has raised high expectations
84 on future applications.[1–3] Many of these properties are superior to those of other materials, but
85 most importantly, the combination of all these characteristics is exceptional. It is of no surprise
86 that GRMs are currently being explored for a multitude of applications, such as in electronics,
87 energy, photonics, composite, filtration, sensors, or biomedicine.[4] As a result of the increased
88 demand, production of GRMs has increased from 14 tons in 2009 to nearly 1,200 tons per year
89 within just a decade. By 2025, the market value is projected to reach between ~US$180 million to
90 US$2.1 billion per year,[5,6] with about 30% of the annual growth rate for graphene reinforced
91 composites.[5]

92 In this respect, GRMs have been proposed as alternative fillers (*i.e.*, materials added in the polymer
93 matrix to improve specific properties) in polymer composites to replace conventional filler agents,
94 such as carbon black and carbon fibers, for reinforcement purpose.[7] More specifically, graphene
95 oxide (GO) and reduced graphene oxide (rGO) are ideal for polymer composites due to their high
96 dispersibility and the presence of functional groups that have chemical affinity to the surrounding
97 polymers and increase filler/matrix adhesion.[4,7] Several studies have shown that the addition of
98 small GRM amounts (0.1-5%) can significantly enhance the strength, electrical conductivity or
99 thermal transport of the composites compared to the neat polymer matrix.[8–12] Among the different
100 polymer matrices, polyamide 6 (PA6, also known as Nylon-6), a widely used engineered
101 thermoplastic polymer, has received great attention, as an ideal matrix for the development of
102 graphene-reinforced polymer composites.[13,14] Its attractive properties, such as good processability,
103 heat and chemical resistance together with its beneficial mechanical characteristics, *i.e.,* stiffness
104 and toughness, make PA6 appealing for composite applications (*e.g.,* automotive and sports
105 equipment).[14,15] Despite its exciting characteristics, PA6 has poor dimensional stability, low
106 electrical conductivity, and weak mechanical performance in some areas, which can all be
107 considerably improved by the use of GRMs as nanofillers.[16–18]

108 Although GRMs may provide solutions to current challenges in many fields, the inevitable
109 occupational or consumer exposure to these materials has raised scientific and public concern for
110 their potential to affect human health. As a result, various studies have been initiated to assess the
111 safety of GRMs in different biological systems, with the reported investigations often showing
112 contradictory or inconclusive results. Several cellular and animal studies with different
113 experimental setups have shown that different types of GRMs can induce mitochondrial
114 dysfunction, cell apoptosis, genotoxicity, inflammatory or oxidative stress responses[19–22], while
115 others reported the absence of adverse effects[23–25] as reviewed by Fadeel *et al.*[26] Overall, this

116 diversity in research outcomes indicate that GRMs are an incredibly diverse family of materials,
117 whose safety thresholds is dependent on the complex interplay of several physicochemical
118 properties such as lateral dimension, thickness, oxidative state, functional groups, dispersion state,
119 purity, administrative doses, exposure route and duration.[27,28] Despite the large number of studies
120 addressing the potential impact of GRMs on human health, knowledge gaps on their structure-
121 activity relationships remain. At present, no classification system exists to determine the exact
122 level at which each material property may contribute to GRM toxicity. Thus, GRM hazard
123 assessment prediction based on physicochemical characteristics is precluded.

124 It is further acknowledged that during the life cycle (production, use, disposal) of GRM-reinforced
125 composites, possible degradation of the solid polymer matrix, *i.e.,* through mechanical abrasion,
126 hydrolysis, water exposure, elevated temperatures or increased UV light intensity, can potentially
127 lead to GRM release and subsequent unintentional exposure of workers and/or consumers.[29–33]. In
128 contrast to pristine GRMs, which have been extensively studied, the nanosafety assessment of
129 materials released from GRM-containing products have not been yet explored and only limited
130 information is available about intrinsic hazards of dissociated materials from graphene-based
131 composites. Moreover, GRMs used as nanofillers in composites may be transformed during the
132 manufacturing process and/or during abrasion process in terms of their physicochemical
133 characteristics such as lateral dimension, thickness, and defects. As a result, the transformed GRMs
134 may cause different biological responses when compared to their pristine form.

135 The aim of the present study was therefore to investigate the potential biological effects of particles
136 released from a real-life GRM-enabled product (*i.e.*, rGO-reinforced PA6 composites that will be
137 soon found in the vehicle industry) through an abrasion process, and compare these effects to those
138 induced by the rGO initially incorporated in the PA6 thermoplastic polymer matrix. Since GRMs
139 and nanomaterials in general, can enter the human body *via* different routes (*i.e.*, inhalation,
140 ingestion, or dermal absorption)[26,34,35] we performed a multi-system and multi-endpoint *in vitro*
141 human toxicity analysis (Figure 1). Using well-established cell lines and cell-type specific
142 endpoints, we first assessed the impact of abraded rGO-reinforced PA6 (PA6-rGO) composite
143 materials on cells representative of key target organs related to the three main exposure routes (*i.e.,*
144 lungs, gut, and skin), and the immune system, our primary defense mechanism against foreign
145 intrusion. As inhalation of airborne materials is a major concern at the workplace where such
146 GRM-enabled products are likely to be processed, we further assess the possible effects of PA6-
147 rGO composite materials on the lungs after single pulmonary exposure in mice. Based on this
148 tiered approach combining *in vitro* and *in vivo* data, the objective of the present study was to
149 provide a comprehensive, multi-laboratory hazard assessment of commercial GRM-enabled
150 products at doses expected at the workplace.

151
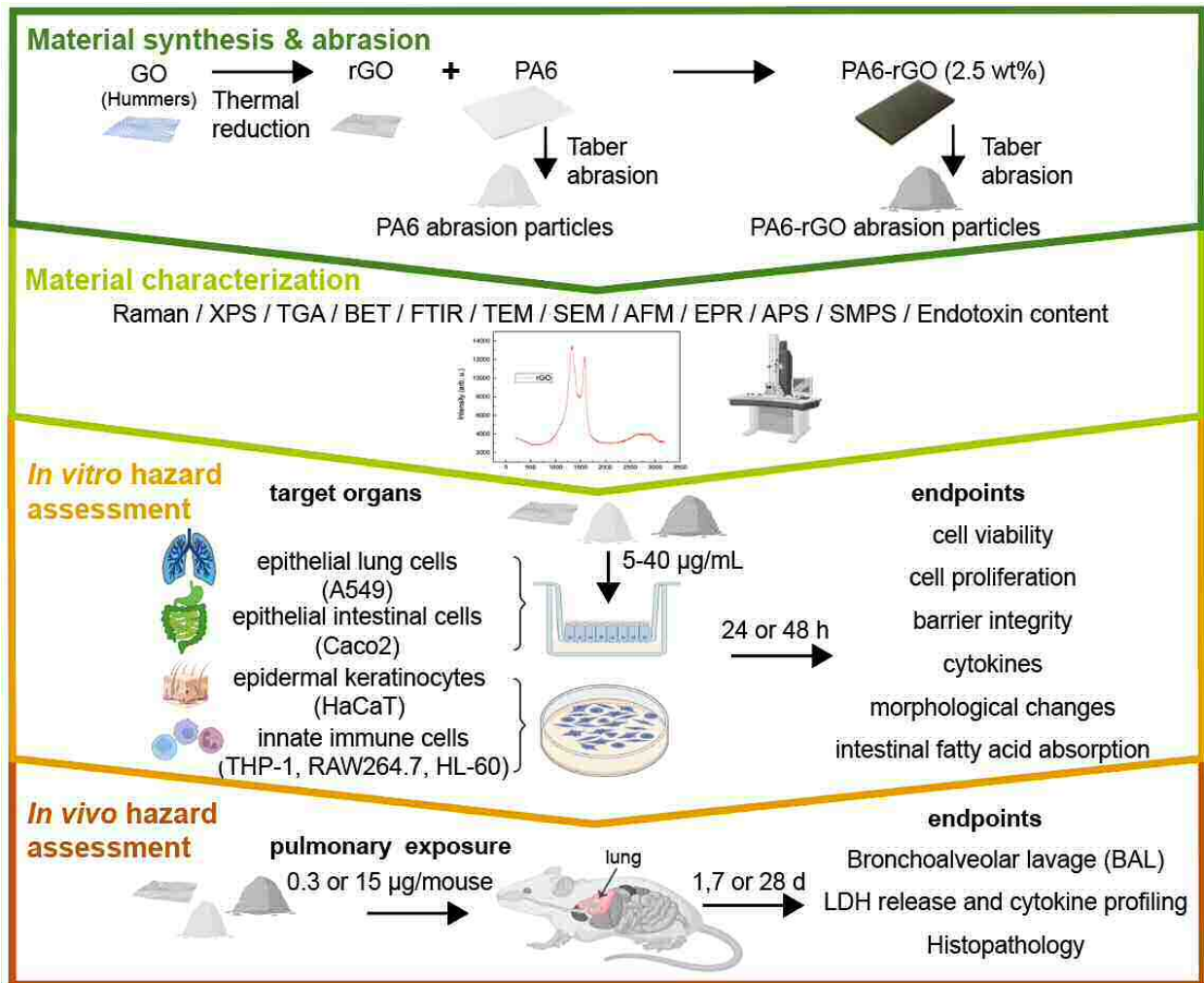
Figure 1. Schematic overview of the experimental strategy. The main steps in the study include: 1) Material generation where rGO is produced by thermal reduction from GO dispersions synthesized by the modified Hummers method. Then, rGO is functionalized with aminopropyl silane and used to generate an industrially relevant rGO-reinforced polyamide 6 composite (PA6-rGO; 2.5 wt% rGO). Abrasion particles are produced from neat PA6 and PA6-rGO by Taber abrasion to mimic a mechanical abrasion. 2) Extensive material characterization is performed using a wide spectrum of analytical methods to support data interpretation and comparability across studies. 3) *In vitro* hazard assessment of the different materials is conducted in robust and widely used cell models representing potential key target organs including the lung, intestine, skin and immune system. 4) *In vivo* hazard is assessed in mice with a focus on short- and long-term toxicity in the lungs, representing the most relevant exposure route. Finally, all the data is carefully analysed in order to achieve a better understanding of the health hazard of abraded PA6-rGO *versus* rGO alone (parts of the figure were created with Biorender.com)

Materials and Methods

Chemicals and Reagents

All chemicals and reagents used were obtained from Merck-Sigma-Aldrich (Switzerland), unless otherwise stated.

Production and characterization of rGO and PA6/PA6-rGO composites

GO preparation

GO dispersion was prepared using the modified Hummers method, using natural graphite sieved at 60 and 100 mesh as described by Eckmann and colleagues.[36] The GO water dispersion was ultracentrifuge at 20.000 rpms in a SIGMA3-30K ultracentrifuge, and the wet solid was collected and filtered off and air-dried.

rGO preparation and functionalization

GO powder was thermally reduced in argon atmosphere at 200ºC for 20 min. Aminopropyl silane functionalized rGO was prepared as follows; Ten g of rGO was suspended in a mixture of ethanol/water (30/70) and stirred for 1h. Concentrated hydrochloric acid was added to adjust pH between 3-3.5. Five mL of (3-aminopropyl) triethoxysilane (APTES) were added and the mixture was stirred overnight at 60ºC. The suspension was vacuum filtered and washed with ethanol to avoid free silane molecules. The powder was dried at 80ºC for 24 h.

Preparation of PA6-rGO composites and characterization

For the preparation of the concentrated masterbatches, an Alphatech AD30mm LD48 counter rotating twin screw extruder was utilised. The functionalised rGO (2.5 wt%) was dispersed in PA6 by melt compounding, resulting in concentrated master batches. The screw speed was kept at 125 rpm and the feeder speed at 30 rpm.

The process temperature in the different barrels in extrusion processes are presented in Table 2.

Extruder zones	Z1	Z2	Z3	Z4	Z5	Z6	Z7	Z8	Z9	Z10
Temperature (ºC)	190	190	210	210	210	220	220	220	220	230

Table 2. Temperatures of the different extruder zones, during melt compounding

The extruded material was then compression moulded to form the film for the abrasion.

Raman Spectroscopy. Raman spectra of rGO and composite materials (before abrasion) were acquired on a confocal RENISHAW in *via* Raman microscope at room temperature. The system uses a CCD detector and a holographic notch filter, using excitation wavelength of 532 nm. Scans were acquired from 1000 to 3500 cm^{-1}, performing maps of 25 spectra and making an average

196 spectrum which is the one that is presented in this paper. Analysis and deconvolution of spectra
197 were obtained with Wire 4.2 software.

198 *X-ray Photoelectron Spectroscopy.* XPS analysis was performed in a KRATOS Axis Ultra DLD.

199 *Fourier-transform infrared spectroscopy.* Infrared spectra were recorded in the 4000–450
200 cm−1 range using a PerkinElmer FT-IR Spectrum Two spectrometer.

201 *Thermogravimetric analysis.* TGA was performed in a METTLER TOLEDO TGA/SDTA 851e
202 in the range of 25-900 ºC 10º/min at air atmosphere.

203 *Brunauer-Emmett-Teller.* The specific surface area (SSA) of GRMs was determined by BET using
204 an autosorb-6 Quantachrome instruments. The samples were degassed in an autosorb degasser
205 (Quantachrome instruments) at 250 ºC for 8 h.

206 *Transmission electron microscopy.* TEM were recorded using a JEOL microscope (JEM-2010).
207 GRM samples were dispersed in isopropyl alcohol then sonicated with a Hielscher UP200S
208 sonicator for 15 min and drop casted onto copper grids for TEM.

209 **Characterization of rGO and abraded particles**
210 *Scanning Electron Microscopy.* The morphology of rGO powder and abraded particles was
211 characterised using an SEM Zeiss Evo50 microscope (acceleration voltage of 10 kV). The powders
212 were deposited on conductive carbon tape and a thin layer of gold ($\approx$ 10 nm) was sputter-coated
213 on top of the samples.

214 *Atomic Force Microscopy.* AFM images were collected by a contact mode (Bruker, Dimension-
215 Icon) to analyze the thickness of the tested materials. Images were obtained using ScanAsyst-Air
216 probes (silicon tips on silicon nitride cantilever, Bruker) with 0.4 N/m nominal spring constant of
217 the cantilever. For the AFM visualization, rGO, PA6 and PA6-rGO were dispersed *via* sonication
218 (10 min) to ethanol. The rGO flakes were then coated to Si/SiO_2 (300 nm) substrate using spin
219 coating method.

220 *Optical Microscopy.* For the optical measurements a Nikon Eclipse LV150N - Digital imaging
221 combined with an advanced optical system was employed.

222 *Raman Spectroscopy.* Raman spectra of the samples were obtained using a Renishaw inVia Raman
223 spectrometer equipped with a 514 nm laser. Four different spectra were acquired in different
224 locations of the samples giving consistent results.

225 *EPR spectroscopy.* EPR spectra were recorded with an ESP 300E spectrometer (Bruker) operating
226 at X-band and equipped with a high sensitivity resonator (4119HS-W1). Spectra were recorded
227 with 2 mW microwave power, a modulation frequency of 100 kHz, a modulation amplitude of 0.1
228 mT, a conversion time of 81.92 ms and time constant of 20.48 ms.

Fluorescence spectroscopy. The presence of ROS in PA6, rGO and PA6-rGO dispersed in 0.1% BSA (at a concentration of 40 µg/mL) was assessed following the fluorescence changes of dihydrorhodamine 123 (DHR123, Sigma-Aldrich) signals using a Jasco FP8003 fluorimeter equipped with a swig xenon 450 W lamp. The non-fluorescent DHR123 is oxidized by ROS to fluorescent rhodamine 123 leading to a significant increase of photoluminescence. In a typical assay, PA6, rGO and PA6-rGO were prepared in 0.1% BSA (1.0 mg/mL) and stocked in the 4 for one week. Then, the stock solutions (80 µL) were diluted with a 0.1% BSA solution (1920 µL) to 40 µg/mL, following the addition of DHR123 (0.4 µL of a stock solution at 1 mM in DMSO) (final concentration of DHR123 corresponding to 200 nM). The fluorescence spectra were recorded immediately (<1 min) and 10 min after adding DHR123 under the excitation at 500 nm and were corrected for the baseline and the solvent. The fluorescence signal of 0.1% BSA following the addition of DHR123 was also tested at 0 min. A Fenton reaction was performed as a positive control. A 200 µL stock solution (10 mM) of the $FeSO_4 \cdot 7H_2O$ was added to 1.6 mL of water followed by 0.4 µL of DHR123 (final concentration of DHR123 corresponding to 200 nM) and 200 µL H_2O_2. For this positive control, the fluorescence spectra were recorded immediately (<1 min) and 10 min after adding H_2O_2.

Abrasion process and particle collection

The abrasion process was performed as described by Netkueakul *et al.*[62] Briefly, PA6 and PA6-rGO composites were abraded using a Taber abraser (Model 5135, Taber, North Tonawanda, NY) equipped with a S-42 sandpaper strip wrapped around a CS-0 wheel with an applied weight of 1 kg to simulate the sanding process on the surface of the composites. The released particles were collected on 0.2 µm nucleopore filter (Whatman, UK) *via* a vacuum inlet (flow rate 10 lpm) with a small suction area of 40 mm^2, connected to conductive silicon tubing (TSI, United States).

Particle Size Distribution. The particle size distribution of the release particles was measured online using an APS (Model 3321, TSI) and a SMPS consisting of a differential mobility analyser (DMA) (Model 3080, TSI, Shoreview, MN) and a condensation particle counter (CPC) (Model 3775, TSI). The flow rate was generated by the vacuum line and monitored in the range of 9 to 11 L/min using a mass flow controller (Model GFM37, Aalborg, NY). In the present experimental setup, the APS analysed the aerodynamic diameter of particles in the range of 0.5-20 µm, while the SMPS analysed particles with electrical mobility diameter ranging from approximately 10 to 570 nm. At least three particle size distributions measurements were collected from each sample. The collection of abraded particles for nanosafety analysis and for further material characterization was performed without the APS and SMPS to reduce possible particle loss.

Material dispersion

For all experiments, freshly prepared stock dispersions of the tested materials (rGO, abraded PA6 and PA6-rGO particles) of 0.5 mg/mL in 0.1% bovine serum albumin (BSA) were prepared by sonication for 45 min prior to usage. Stock dispersions were diluted to the final working

266 experimental concentrations (2.5-40 µg/mL) in complete cell culture medium and used
267 immediately for exposure experiments.

Endotoxin content

Endotoxin Chromogenic assay

270 The endotoxin concentration in PA6, PA6-rGO and rGO suspensions was measured using the
271 Pierce™ LAL Chromogenic Endotoxin Quantitation kit (sensitivity 0.1 EU/mL; Thermo Fisher
272 Scientific, MA, USA), following the manufacturer's instructions, at concentrations 0-80 µg/mL.

TET Assay

274 PA6, PA6-rGO, and rGO samples were assessed for endotoxin content with the TNF-α expression
275 test (TET), which enables unequivocal detection of endotoxin with a sensitivity comparable to that
276 of the conventional LAL assay but without any interference with the assay. In brief, PBMCs were
277 isolated from buffy coats obtained from healthy human blood donors (Karolinska University
278 Hospital, Stockholm, Sweden) by density gradient centrifugation, as described previously.[143]
279 Then, PBMCs were positively selected for CD14 expression with CD14 MicroBeads (Miltenyi
280 Biotech, Bergisch Gladbach, Germany). For obtaining HMDMs, CD14+ monocytes were cultured
281 in RPMI-1640 cell medium supplemented with 2 mM L-glutamine, 100 IU/mL penicillin, 100
282 mg/mL streptomycin, and 10% heat-inactivated fetal bovine serum (FBS), supplemented with 50
283 ng/mL recombinant macrophage colony-stimulating factor for 3 days in 96-well plates.[122]
284 HMDMs were exposed to PA6, PA6-rGO, and rGO (20 g/mL) or to bacterial LPS (0.01 µg/mL)
285 (Sigma-Aldrich) in the presence or absence of the specific LPS inhibitor, polymyxin B (10 µM)
286 (Sigma-Aldrich), and TNF-a secretion was measured at 24 h of exposure with a Human TNF-α
287 ELISA Kit purchased from MABTECH (Nacka Strand, Sweden).

Detection of released graphene from PA6-rGO abraded composites

Freeze fractured samples and SEM visualization

290 As the release of rGO could be explained by the debonding of the rGO from the PA-6 matrix,
291 freeze fractured method was employed to simulate the debonding process and to explain the
292 debonding mechanism. In order to generate the freeze fractured surface, the sample was immersed
293 into liquid nitrogen for 30 s. After removing the sample from liquid nitrogen, the sample was
294 immediately broken by manual bending. Freeze fractured surface of the samples was analyzed
295 using scanning electron microscope (Nova NanoSEM 230, FEI company, Hillsboro, OR, USA).

Transmission electron microscopy of abraded PA6-rGO

297 It was important to evaluate whether abrasion process could induce the release of the rGO from
298 the polymer matrix or not. If the rGO can be released, it is also crucial to assess in which forms
299 rGO was released. Therefore, to understand the characteristics of rGO in the abraded PA-6-rGO,
300 the abraded PA6-rGO was analyzed using TEM (FEI Tecnai G2 F20 (FEI Company, OR, USA)).

In vitro experiments and post-exposure biological response

Cell cultures

Lung cultures

Human A549 epithelial type II cells were obtained from American Type Culture Collection (ATCC; Virginia, USA). After thawing, A549 cells were sub-cultured in T75 cell culture flasks in complete Rosewell Memorial Park Institute medium (RPMI-1640, Sigma-Aldrich) with 10% FBS (Sigma-Aldrich), 1% penicillin, streptomycin, neomycin (PSN; Sigma-Aldrich) and 1% L-glutamine (Sigma-Aldrich). Cells were maintained at 37 °C and 5% CO_2 in humidified atmosphere and were routinely sub-cultured twice a week at 70–80% confluence.

Prior to the experiments, cells were seeded apically on transparent polycarbonate 12-well inserts (3 μm pore size, 113.1 mm^2 surface area, Greiner Bio-One, Austria) at concentration of 2.5×10^5 cells/insert and were grown for three days on submerged conditions to form a tight monolayer, Cell cultures were then transferred to air-liquid interface (ALI) conditions by removing the apical medium in order to produce surfactant and better reflect *in vivo* conditions in human lung.[70] After 24 h at ALI, cells were then exposed apically to 100 μL of different concentrations of PA6, PA6-rGO and rGO (2.5-40 μg/mL), for 24 h and 48 h (pseudo-ALI approach[71,72]).

Crystalline quartz DQ (purchased from Dörentrup Quarz GmbH & Co. (material No. 04; mean particle diameter d(50)= 3.71 μm, d(97)=12.03 μm)) was included as a positive inflammogenic control for A549 cells. DQ was freshly dispersed in ultrapure ddH$_2$O, and 100 μL were applied apically in A549 cells (final concentration of 100 μg/mL).

Skin cultures

HaCaT cells were cultured in high glucose Dulbecco's Modified Eagle's medium (DMEM), supplemented with 10% FBS, 1.0×10^{-2} M L-glutamine, 1.0×10^{-4} g/mL penicillin and 1.0×10^{-4} g/mL streptomycin at 37°C in a humidified (95%; air: 5% CO_2) atmosphere. Cell passage was performed two days post-confluence, once a week. All the experiments were performed between passage 74 and 86. For cytotoxicity assays, cells were seeded in flat bottom 96-well plates at a density of 5×10^3 cells/well and exposed to different concentrations of the tested materials (2.5-40 μg/mL) for 24 h and 48 h. Before each assay, cells were washed twice with phosphate buffered saline (PBS).

Intestinal cultures

The human colorectal adenocarcinoma cell line Caco-2 was obtained from the German collection of microorganisms and cell cultures (DSMZ, Braunschweig, Germany). Cells were maintained in Minimum Essential Medium (MEM; Sigma-Aldrich) supplemented with 10% FBS, 2 mM L-glutamine (Sigma-Aldrich), 1% PSN (Sigma-Aldrich) and 1% non-essential amino acids (Sigma-Aldrich) Cell cultures were maintained at 37 °C, 5% CO_2 and 95% humidity and routinely sub-cultured twice a week at 70–80% confluence using 0.5% trypsin–EDTA (Sigma-Aldrich).

Differentiation of intestinal cells. Caco-2 cells were seeded at a density of 250,000 cells/well (corresponds to $2.2×10^5$ cells/cm^2), in ThinCert™ cell culture inserts for 12-well plates (high pore density transparent PET membrane, with 3 µm diameter pore size; Greiner bio-one, Kremsmünster, Austria). Cells were grown for 21 days to obtain mature differentiated monolayer and cell culture medium was refreshed three times per week. At day 22, cells were treated with different concentrations of the tested materials at a range of 2.5-40 µg/mL (100 µL of particle suspension, added apically), for 24 h and 48 h.

Immune cell cultures

The human monocytic THP-1 cell line was purchased from the ATCC (Virginia, USA). Cells were grown in RPMI 1640-GlutamaxTM-I media containing HEPES (Gibco, Sweden) and supplemented with 100 U/mL penicillin, 100 mg/mL streptomycin and 10% heat-inactivated FBS (Sigma). The cells were passaged at a cell density of up to maximum $8.0×10^5$/mL every 3–4 days.

Differentiation of THP-1 cells. For the experiments, the THP-1 cells were plated at the cell density of 60,000 cells/well and pre-incubated for 24 h in the presence of 0.5 µM PMA, as described previously.[144] After 24 h the differentiated THP-1 cells were washed with luke-warm sterile PBS and exposed to rGO, PA-6-rGO and PA-6 (concentrations 5-40 µg/mL) for 24 h. Cells were tested regularly using MycoAlert® mycoplasma detection kit (Lonza, Basel, Switzerland). Cells were seeded in 96-well plates in RPMI-1640 medium at a density of 60000 cells/well and subsequently exposed to the tested materials at concentrations 5-40 µg/mL for 24 h, or were maintained in cell medium alone (untreated cells-negative control).

The RAW 264.7 macrophage cell line was cultured in DMEM cell culture medium supplemented with 10 µg/mL gentamycin, 10 mM N-(2-hydroxyethyl)-piperazine- N-ethanesulfonic acid, 0.05 mM β-mercaptoethanol and 10% FBS at 37°C in a 5% CO_2 incubator. Cells were seeded in 96-well plates at a density of $1×10^4$ cells per well and cultured for 24 h prior the material exposure. The human acute promyelocytic leukemia cell line HL 60 (ATCC – CCL 240) was maintained in phenol red free RPMI 1640 medium supplemented with 2 mM l glutamine and 10% heat inactivated FBS (Sigma) in 5% CO_2 at 37°C.

Differentiation of HL-60 cells. In order to allow for neutrophil like differentiation, the cells were seeded at $0.5×10^6$ cells/mL in the above mentioned cell medium supplemented with 1.25% DMSO for 5 days, as described previously.[145] The culture medium was refreshed after 3 days. Cells were tested regularly using MycoAlert® mycoplasma detection kit (Lonza, Basel, Switzerland). Prior the exposure, experiments the differentiated HL-60 cells were seeded in 96-well plates in phenol red-free RPMI-1640 medium at a density of 60000 cells/well.

After seeding, the immune cells were treated with the indicating concentrations (5, 10, 20, 40 µg/mL) of PA6, PA6-rGO and rGO and the biological response was evaluated 24 h post-exposure.

Cell viability

MTS assay

The effects of the materials on cell viability were evaluated by the 3-(4,5-dimethylthiazol-2-yl)-5-(3-carboxymethoxyphenyl)-2-(4-sulfophenyl)-2H-tetrazolium (MTS) assay (CellTiter 96® AQueous One Solution Cell Proliferation Assay, Promega, Dübendorf, Switzerland) in all the cell models examined (with the exception of the neutrophil model, where the ATP assay was performed instead), according to ISO 19007:2018 and.[146] Briefly, after material exposure, phenol red free fresh medium containing the MTS reagent was added to the cells. Then, the cell cultures were incubated for an additional 1 h (4 h for the skin model), at 37°C. Absorbance was measured at 490 nm by a microplate reader. The chemical positive control cadmium sulphate ($CdSO_4$, Sigma-Aldrich) was added to the cells at concentration 1000 µM for 24 h. Data are presented as % cell viability as compared to negative control (untreated cells).

Cell free interference assay was performed for the rGO and the abraded particles, at a concentration range of 0–40 µg/mL to exclude potential interference reactions of the tested materials with the MTS assay reagents along that might lead to possible wrong interpretation of the results (SI 15).

ATP assay

The ATP assay was performed for the viability assessment of the neutrophil model. After the 24 h material exposure, the differentiated HL-60 cells were lysed, and total cellular ATP content was quantified with a luminescence-based cell viability assay, CellTiter-Glo (Promega, Dübendorf, Switzerland). CellTiter-Glo reagent was mixed at a 1:1 ratio with the experimentally treated cells from the treatment plate. The mix was incubated for 10 min at room temperature on the shaker, followed by luminescence measurement with an Infinite F200 Tecan plate reader (Mannendorf, Switzerland). The experiment was performed with at least three biological replicates and three technical replicates for each concentration of PA-6, PA6-rGO, and rGO. Results were expressed as percentage cell viability *versus* control.

To control for potential interference of the materials with the assay, the PA-6, PA6-rGO and rGO were dispersed in cell-free medium (at the working concentrations) and mixed with CellTiter-Glo reagent (no interference was observed; data not shown).

WST-8 assay

The cell viability in skin cells was additionally evaluated by the 2-(2-methoxy-4-nitrophenyl)-3-(4-nitrophenyl)-5-(2,4-disulfophenyl)-2H-tetrazolium (WST-8) reduction assay. The WST-8 assay was carried out using the Cell Counting Kit (CCK)-8 assay (Sigma Aldrich; Milan, Italy), as previously described [100]. Briefly, after materials exposure and two washings with PBS, cells were incubated for 4h with fresh medium containing 10% WST-8 reagent. Absorbance was determined at 450 nm by an Automated Microplate Reader EL 311s (Bio-Tek Instruments; Winooski, VT). Data are reported as % cell viability as compared to negative control (untreated cells).

LDH assay

The potential cytotoxicity in RAW 264.7 macrophages was assessed by the LDH test kit (CytoTox 96® Non-Radioactive Cytotoxicity Assay, Promega, Dübendorf, Switzerland), according to the

manufacturer's instructions. Following the 24 h post-exposure time, the culture medium was collected for the LDH measurements. Treatment of cells for 30 min with lysis solution (included in the assay) was served as positive control to induce cytotoxicity. The OD of each sample was recorded at 490 nm on a Microplate Reader (Thermo, Varioskan Flash). LDH release (% of positive) is presented as the percentage of $(OD_{test}-OD_{blank})/(OD_{positive}-OD_{blank})$, where OD_{test} is OD of control cells or cells exposed to materials, $OD_{positive}$ is OD of positive control cells and OD_{blank} is OD of well without cells.

Evaluation of intestinal barrier integrity

The differentiation process of Caco-2 cultures grown in 12-well inserts was controlled by TEER measurements at day 7, 14 and 21 after seeding using an Epithelia Voltohmmeter (EVOM) with sterilised STX2 electrodes (World precision, Instruments, Sarasota Florida, USA). The impact of different concentrations of PA6, PA6-rGO and rGO (2.5-40 µg/mL) on the barrier integrity of differentiated Caco-2 cells was assessed by measuring the TEER before the treatment (0 h) and after 24 h and 48 h of treatment. Three measurements in different parts of the insert were retrieved from each sample, and TEER values were calculated using the formula TEER = [Ω (cell inserts) – Ω (cell-free inserts)] × 1.12 cm^2. The values for each concentration represent the average of three independent experiments.

Lipid absorption on the intestinal barrier

To investigate the potential effects of rGO and abraded PA6/PA6-rGO particles on lipid uptake, differentiated Caco-2 cells on 12-well inserts were exposed with different concentrations of each tested material (5-40 µg/mL) for 24 h and 48 h. Cell cultures treated with 50 µg/mL of the fatty acid synthase inhibitor C75 for 24 h were used as a positive control. Lipid uptake was measured as described in previous work.[97] Briefly, after material exposures, the cultures were incubated for 10 min with 20 µM BODIPY™ 500/510 C1, C12 (Thermo Fischer, D3823) in 0.1% BSA, according to the manufacturer's instructions. Then, the inserts were washed with ice cold 0.1% BSA and complete DMEM medium (phenol red free) was added to the apical and basolateral side. After 1 h incubation at standard growth conditions, the fluorescence was measured with a multi-well plate reader (Mithras2 Plate reader, Berthold Technologies, Germany) at 485/528 nm (excitation/emission).

Skin cell mass and proliferation

Cell mass was evaluated by the sulforhodamine B (SRB; Sigma Aldrich, Milan, Italy) assay, as a measure of viable adhered cells.[104] Briefly, after materials exposure, cells were washed twice with PBS, fixed with 50% trichloroacetic acid for 1 h at 4°C and stained for 30 min with 0.4% SRB in 1% acetic acid. After washings with 1% acetic acid, the protein-bound dye was dissolved in 10 mM TRIZMA base solution and the absorbance was read by an Automated Microplate Reader EL 311s (Bio-Tek Instruments, Winooski, VT, USA) at 570 nm. Data are reported as % of cell mass with respect to negative control.

449 Cell proliferation was evaluated using a colorimetric ELISA based on 5-bromo-2′-deoxyuridine
450 (BrdU) incorporation (Sigma-Aldrich; Milan, Italy), following the manufacturer's instructions.
451 Absorbance was read by an Automated Microplate Reader EL 311s (Bio-Tek Instruments,
452 Winooski, VT, USA) at 450 nm. Data are reported as % of cell proliferation with respect to
453 negative control.

Inflammatory responses (lung and immune cells)

Cytokine and chemokine release
456 The secretion of human IL-6 and IL-8 in A549 alveolar epithelial cells (24 h and 48 h post-
457 exposure to rGO and abraded composite materials) was quantitatively detected by enzyme-linked
458 immunosorbent assay (ELISA; Human IL-6 and IL-8 Uncoated Elisa Kit, Invitrogen, USA)
459 according to manufacturer's instructions. Cells treated apically with 1 µg/mL TNF-α for 24 h were
460 used as positive control. Measurements were performed on high binding 96-well plates (Coating
461 Costar, New-York, USA) and at 370 nm optical absorbance using a microplate reader (Mithras 2
462 Plate Reader, Berthold Technologies, Germany).
463 Differentiated THP.1 were exposed to rGO (20 µg/mL). The exposed cell media were collected
464 and stored at -80°C for further analysis. IL-1β release was determined by using a human IL-1β
465 ELISA kit (Invitrogen, Sweden) according to the manufacturer's instruction. Absorbance was
466 measured at 450 nm using a Tecan Infinite F200 plate reader. Results are expressed as pg/60 000
467 cells of released cytokine. To assess the role of the NLRP inflammasome, cells were preincubated
468 for 1 h with either zVAD-fmk (20 µM) and MCC950, an NLRP3 inhibitor (10 µM) (both from
469 Sigma).
470 The release of TNF-α (BD OptEIA, BD Biosciences) and IL-6 (BD OptEIA, BD Biosciences) in
471 RAW 264.7 macrophages, following 24 h treatment with the tested materials was determined using
472 ELISA kits (BD Biosciences), following the manufacturer's instructions. Optical absorbance
473 measurements were performed using a microplate reader (Thermoscientific, VARIOSKAN LUX)
474 at 450 nm. LPS (1 µg/mL for 24 h, Sigma) served as the positive control to stimulate inflammatory
475 response.

Multiplex analysis-based cytokine profiling on immune cells
477 The Meso Scale Discovery (MSD) (Rockville, MD, USA) plate-based electrochemiluminescence
478 (ECL) assay was employed to quantify cell supernatant concentrations of IFN-γ, IL-1β, IL-2, IL-
479 4, IL-6, IL-8, IL-10, IL-12 p70, IL-13, and TNF-α. As a positive control, cells were exposed to
480 0.1 µg/mL LPS for 24 h. The stored cell supernatant was thawed on wet ice just prior to use.
481 Samples were diluted 1:2 using Diluent 2, and each sample was run in duplicate. The V-PLEX
482 Human Pro-inflammatory Panel 1 Human Biomarker 10-Plex Kit was used. Plates were processed
483 according to the manufacturer's instructions and read using the MSD MESO Sector S 600
484 instrument. The assay data were analyzed using MSD Discovery Workbench 4.0. The cytokine
485 expression data retrieved from the multiplex assay were analyzed using hierarchical clustering
486 analysis. Complete linkage and Euclidean distances were employed as metrics to draw association

487 dendrograms between cytokines and the different treatment conditions, as described previously.[144]
488 The cluster analysis and the corresponding heat maps were prepared by using R, as previously
489 reported.[144]

Cell morphology

491 Following the 24 h and 48 h material exposure, A549 alveolar epithelial cells were fixed in 4%
492 paraformaldehyde (PFA) and incubated at 4°C. In order to prepare the cells for staining, cultures
493 were incubated with 0.1 M glycine in PBS for 15 min. Then, cells were permeabilized with 0.2%
494 Triton X-100 in PBS for another 15 min, prior the application of fluorescent dyes. DAPI (4′,6-
495 diamidino-2-phenylindole) (Thermo Fischer, USA), and Alexa Fluor 488 (Thermo Fisher, USA)
496 were used to stain nuclei and cytoskeleton of the cells respectively. DAPI and Alexa Fluor 488
497 were diluted to ratio of 1:1000 and 1:50 respectively in 0.3% Triton X-100 and 1g BSA in PBS.
498 Following the staining, cells were incubated with fluorescent dyes for 1.5 h in darkness, at room
499 temperature. Subsequently, cells were washed three times with PBS and mounted on microscopy
500 slides using Mowiol® 4–88 (Sigma-Aldrich) on both sides of the membranes. Visualization of the
501 cellular morphology was achieved using a confocal LSM fluorescence microscope (CLSM,
502 LSM780, 60× magnification oil, Carl Zeiss AG, Switzerland).
503 The morphology of keratinocytes was evaluated by confocal microscopy after membranes staining
504 with 1 μM 1,1'-Dioctadecyl-3,3,3',3'-tetramethylindocarbocyanine perchlorate (DiL) probe
505 (Sigma-Aldrich; Milan, Italy), as previously described.[104] Cells (2×10^5 cells/well) were cultured
506 for 24 h before exposure to each material (40 μg/mL) for 48 h. Cells were then washed twice with
507 PBS, probed with 1 μM DiL for 10 min at room temperature, fixed with 4% PFA for 30 min at
508 room temperature and washed twice with PBS. Samples were mounted on coverslips of 1 mm
509 thickness using the Prolong Gold antifade reagent (Life Technologies; Milan, Italy). Images were
510 taken by a confocal microscope (Eclipse C1si, on an inverted microscope TE2000U, Nikon) at
511 60× magnification. GBMs presence in each sample was visualized by the reflection mode property
512 during the confocal acquisitions. Reconstructions of the images were performed offline using the
513 image-processing package Fiji.

514 RAW 264.7 macrophages were plated in the 96-well plates (1×10^4 cells per well) and incubated
515 for 24 h. Abraded materials were added to the cells at increasing concentrations (5, 10, 20, 40
516 μg/mL) upon dispersion in cell culture medium. Untreated cells cultured in cell culture medium in
517 absence of materials were used as negative control. The cell morphology was observed under an
518 optical microscopy (Zeiss Axiovert 40 CFL, 20× magnification) at 24 h post-exposure.

In vivo exposure experiments and post-exposure tissue analyses

Animal husbandry

521 Prior to any experiment, C57BL/6 female mice (Envigo, UK) of 6 to 8-week old were acclimatized
522 for 7 days after arrival. Animals were kept randomized in groups of 5 with free access to water
523 and food, at a temperature of 19°C–22°C, relative humidity of 45%–65%, under a regular 12 h

light/dark cycle between 7 am and 7 pm. All procedures were conducted in accordance with the ARRIVE guidelines for animal research and after ethical approval from the UK Home Office, under Project License no. P089E2E0A.

Animal exposure

All materials were prepared on the day of exposure by dispersion in water (water for injection, ThermoFisherScientific, Gibco) containing 0.1% BSA (Merck, Sigma-Aldrich). After anesthesia with 3% of isoflurane, mice were maintained on a slanted board and 30 µL of materials or vehicle was put at the basis of the tongue, allowing distribution of the materials into the lungs through physiological breathing. Mice (n=3) were exposed by oropharyngeal aspiration to 15 µg (in 30 µL) of PA6-rGO (2.5% of rGO, which represents about 0.3 µg of rGO for 15 µg of PA6-rGO) or controls: neat PA6 (15 µg), rGO-0.3 µg (low dose, representing approximately 2.5% of the high dose) or rGO-15 µg (high dose) and vehicle (0.1% BSA in water). The applied dose of 15 µg per animal equals to 0.75 mg/kg, while 0.3 µg per animal equals to 0.015 mg/kg for animal weighing on average 20 g at the time of exposure. Outcomes were assessed at 1, 7, and 28 days after single exposure. At each time point, mice were euthanized by intraperitoneal injection with an overdose of pentobarbitone.

Bronchoalveolar lavage (BAL) analysis

At the end of the post-exposure recovery period, bronchoalveolar lavages (BAL) were performed on the right lung (isolated *via* litigation of the right bronchia) using 3 times 0.8 mL ice cold PBS (Merck, Sigma-Aldrich). BAL fluids were analyzed for composition in cell population (differential counting by Kwik-Diff Stains, Epredia, Shandon), LDH (LDH colorimetric assay, Promega) and total protein content (Bi-cinchoninic Acid (BCA) assay, Pierce BCA Protein Assays, ThermoFisherScientific). IL-6 and TNF-α concentrations in BAL fluids were assessed using Mouse ELISA MAX deluxe Sets (Biolegend).

Whole lung inflammation profile analysis

After BAL, the right lungs were lysed in RIPA buffer (Merck, Sigma-Aldrich) containing EDTA-free protease inhibitor (cOmplete Mini, Roche). After homogenization using 5 mm stainless steel beads for 10 min at 50 Hz (TissueLyser LT system, Qiagen), cell lysates were centrifuged for 5 min at 2600 g to remove cell debris. Collected supernatants were stored at -80°C until analysis. Total protein concentrations were measured using a BCA assay (ThermoFisherScientific, Pierce), and cytokine levels were evaluated using a Mouse Inflammation Panel (13-plex: IL-1α, IL-1b, IL-6, TNF-α, MCP-1, GM-CSF, IL-17A, IL-23, IL-12p70, IFN-γ, IFN-β, IL-27 and IL-10, v-plate, Biolegend) following manufacturer's recommendations. A FACSVerse flow cytometer (BD biosciences) was used to measure fluorescence intensities. Sample concentrations were determined using a standard curve and then expressed in pg/mg of protein after normalization by total protein concentration. IL-12p70 values were below the test sensitivity and were not considered.

Histopathological analysis

The left lungs were collected, fixed in formalin, paraffin embedded, sectioned on microtome, and finally stained using Hematoxylin and Eosin stain for further histopathological analysis.

Statistical analysis

In vitro results are presented as the mean ± standard error of the mean (SEM) of at least 3 independent experiments, and presented as the mean ± standard deviation for *in vivo* experiments (n=3). Statistical analysis was performed by one-way ANOVA followed by Bonferroni's post-test, Dunnett's or Sidak's multiple comparison test analysis, using the software GraphPad Prism (version 9.0). The results were considered significant if $p<0.05$. For each *in vivo* time point, Kruskall-Wallis followed by Dunn's post-hoc test was used to evaluate statistical differences compared to the negative control; $p<0.05$: *.

Results and Discussion

Characterization of rGO and abraded particles from PA6-rGO composites

The rGO samples were produced by thermal reduction from GO dispersions synthesized using the modified Hummers method.[36] Subsequently, rGO was functionalized with aminopropyl silane. The surface functionalization of rGO was verified by Raman, x-ray photoelectron spectroscopy (XPS), thermogravimetric analysis (TGA), Brunauer-Emmett-Teller (BET) and Fourier-transform infrared (FTIR) analysis. SI 1a presents a comparison of the Raman spectra of the GO, non-functionalized rGO and aminopropyl silane functionalized rGO). An intense D peak (~1350 cm^{-1}) which confirmed lattice distortions and the G peak (~1585 cm^{-1}) which corresponds to the overlap of G and D' peaks are observed. The 2D peak (~2700 cm^{-1}), and D+D' and 2D' peaks which are different overtone and combination peaks of the previous ones, show minimal intensity, corresponding to stage 2 defects. Non-functionalized rGO shows the highest I(D)/I(G) [I(D)/I(G) 1,15 (functionalized rGO), 0,70 (non-functionalized rGO), 0,86 (GO)] in agreement with the evolution of I(D)/I(G) in stage 2 of defects. A decrease in full width half maximum (FWHM) of D and G peaks were observed for non-functionalized rGO material FWHM$_G$: 73 (GO), 103 (non-functionalized rGO), 70 (functionalized-rGO) cm^{-1}; FWHM$_D$: 107 (GO), 186 (non-functionalized rGO), 78 (functionalized-rGO) cm^{-1}, which is associated to a decrease in disorder and in alignment with a decrease of the oxygen content due to a reduction process during the functionalization of rGO.[37–39] The reduction process was further confirmed by XPS where a decrease in the oxygen content was reported: 30.4% (GO), 13.5% (non-functionalized rGO), decreased to 6.7% (functionalized rGO), during the silanization process (SI 2). It should be noted, that the rGO is intentionally a partially rGO, because this characteristic (together with the functionalisation) enables a better integration and improved mechanical properties in the polymer composite for automobile applications. Hence, this rGO is not representative of graphene that would be used in electronics or for conductivity purposes. In the case of functionalized rGO, 0.4% of Si and 0.44%

of N was observed corresponding to a 0.4% of functionalization of the rGO. FTIR spectra of the functionalized rGO in region 620-1300 cm^{-1} showed two width and high intensity peaks, which involved different components typically assigned to Si-O-Si, Si-O-C (1083 and 1047 cm^{-1} is typically assigned to the Si-O-C and Si-O-Si bonds, respectively, and indicates the successful chemical functionalization) and Si-C vibrations (appears at 870 cm^{-1} as broad peak) (SI 1b). Similar patterns were observed by Wan *et al.*[40] TGA revealed a mass loss of 3.9 wt% below 525ºC, in agreement with the 4.3 wt% loss calculated when assuming a degree of functionalisation of 0.4% (SI 3). The starting non-functionalized rGO showed a BET surface area of 736,3 m^2/g, while the functionalised rGO incorporated in the composites, demonstrated a BET surface area of 178,7 m^2/g. The reduction in the surface area is attributed to the non-accessible area of the gases due to the stacking during the filtration and drying process.[41] Transmission electron microscopy (TEM) observed that the functionalized rGO comprised of folded structures and was agglomerated (SI 4). The functionalized rGO was either embedded in the PA6 composites (2.5 wt%) or used for further characterization and toxicological analysis (hereafter, rGO refers to functionalized rGO).
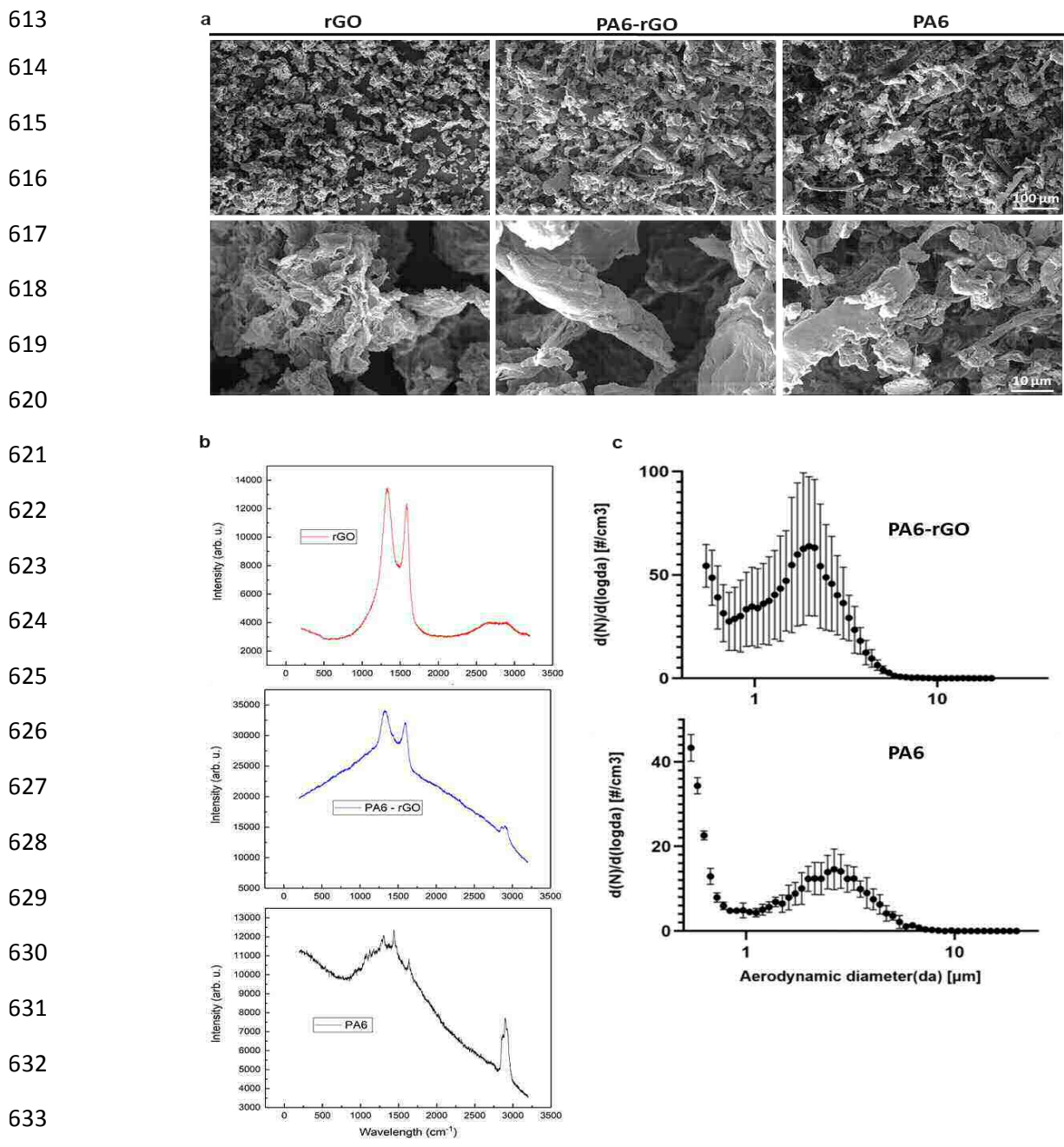
Figure 2. Characterization of rGO and abraded particles from PA6-rGO composites. (a) SEM images of rGO, abraded particles from PA6-rGO composite and abraded particles from neat PA6. (b) Raman spectra of the tested materials (rGO, abraded PA6-rGO and abraded PA6). (c) Particle size distributions of the abraded particles in the micrometer range, measured by APS. The results show mean ± S.D. from at least three independent measurements.

The morphology of the rGO and the abraded composites (PA6 and PA6-rGO) was studied using scanning electron microscopy (SEM), atomic force microscopy (AFM), as well as optical microscopy (Figure 2a, SI 5a-b). The SEM micrographs of the rGO showed aggregated nanoflakes with broad cluster sizes that range from 10 to 100 μm (Figure 2a). Such an arrangement of graphene sheets is typical of rGO powders.[42] Moreover, the large SEM magnification allows distinguishing crumpled nano-scaled flakes of rGO stacked together. The abraded PA6 particles

19

644 form a worm-like structure with morphologies comparable to other previous reports.[43] The abraded
645 PA6-rGO composites display similar worm-like topography with worm sizes in the range of 10-
646 100 μm. The presence of rGO could not be detected by SEM imaging in the abraded PA6 particles.
647 Similarly, Sachse *et al.*, observed that particles generated from PA6-foam glass crystal (FGC),
648 PA6-SiO$_2$ composites after a drilling process, showed very similar structures of particles.[44]

649 AFM was employed to evaluate the thickness of the flakes/agglomerates in the tested materials.
650 Height profiles indicated areas of increased thickness of rGO flakes, which are predominantly
651 stacking or folding on each other (SI 5a). Similarly, in the abraded PA6-rGO, the stacking of
652 several layers was monitored, which is verified by the variation in thickness values. The average
653 thickness for rGO and PA6-rGO was similar (6-10 nm and 4-10 nm, respectively). In addition,
654 AFM showed that lateral dimensions of rGO ranged from 1 to 5 μm, while PA6-rGO ranged from
655 0.75 to 5 μm. Due to difficulties to disperse PA6 to a non-aggressive solvent, it was not possible
656 to achieve AFM measurements for the neat PA6.

657 The presence of rGO in the PA6-rGO composite, after the abrasion process could be confirmed by
658 the presence of the characteristic D and G peaks in the Raman spectra. The Raman spectra of the
659 neat abraded PA6 particles presented a strong fluorescence contribution (Figure 2b). The main
660 peaks of this sample and the correspondent vibration modes were analysed in a previous report.[45]
661 The Raman spectra of the rGO and abraded PA6-rGO were analysed through Lorentzian fitting.
662 The rGO showed the typical D peak at approximately 1335 cm^{-1} and the G at ≈ 1579 cm^{-1}, which
663 is consistent with previous studies (Figure 2b).[46,47] The I(D)/I(G) ratio was ≈ 1.2. The
664 characteristic 2D peak could be observed between 2500 and 2800 cm^{-1}. The abraded PA6-rGO
665 composite instead presented a blue shift of approx. 10 cm^{-1} resulting in a D peak at ≈ 1345 cm^{-1}
666 and a G at 1587 cm^{-1} (I(D)/I(G) was ≈ 1.1).

667 The presence of surface radicals was examined by EPR and fluorescence spectra analysis as
668 reactive oxygen species (ROS) account one of the main drivers for particle toxicity.[48] As reported
669 in the SI 6a, no radicals were observed in the neat PA6, while low amounts of radicals were
670 detected in the rGO containing samples (both powder and dispersed form) with likely no influence
671 on the biological responses in the concentrations tested (SI 6b).

672 The particle size distribution of the abraded composites was measured online, during the abrasion
673 process, using the aerodynamic particle sizer (APS) and the scanning mobility particle sizer
674 (SMPS) that quantify the aerodynamic diameter and the electrical mobility of the abraded particles,
675 respectively. Online APS measurements of the released particles during the abrasion process
676 revealed a mean aerodynamic diameter of 3.16 μm for the neat PA6 and 1.91 μm for the PA6-rGO
677 composite particles (Figure 2c). For both abraded materials, the obtained aerodynamic diameter
678 values were under 4 μm, which falls into the respirable fraction in the alveolar region.[34] More
679 specifically, particles with an aerodynamic diameter smaller than 100 μm can be inhaled, but only
680 particles with an aerodynamic diameter smaller than 4 μm can reach the alveolar region of the
681 lung.[34,49] Another peak was observed towards the lower detection limit of the instrument (at 0.5

682 μm) for both abraded materials, indicating the presence of particles with an aerodynamic diameter
683 smaller than 0.5 μm. It should be noted that the aerodynamic diameter of the abraded particles
684 measured by APS was notably smaller than the particle size estimated by the SEM. This
685 observation, which was reported previously by Schinwald *et al.*, could be explained by the fact
686 that in contrast to the particle size estimated by SEM from the projected area, the aerodynamic
687 diameter measurements depend on both the shape, the density and the orientation of the particles
688 with respect to its direction of motion.[50] Furthermore, the APS results suggested that the addition
689 of 2.5 wt% functionalized rGO in the polymer matrix resulted in a decrease in the average particle
690 size compared to the particles released from the neat PA6. Recent studies have shown that the
691 addition of GRMs at concentrations as low as 0.5 wt% could significantly improve the mechanical
692 properties of polymer composites.[51,52] The presented PA6-rGO composites demonstrated
693 improved mechanical properties as confirmed by the increased Young´s modulus and tensile
694 strength, compared to other GRM-PA6 and neat PA6 composites.[53] This increase in toughness
695 could make the composites more challenging to crack, leading to the generation of smaller
696 particles, as shown in the PA6-rGO. In contrast, the lower hardness of neat PA6 resulted in
697 separation of larger sized particles.[54] In addition, a larger number of particles was collected from
698 PA6-rGO composite samples than from the neat PA6 samples. This could be explained by the
699 observed electrostatic charging in the neat PA6 particles during abrasion and their scattering, prior
700 to their collection by the vacuum probe. Jian *et al.* reported that the electrostatic potential and the
701 tribological behavior of PA6 during a wear process is not a simple mechanism and can be affected
702 by internal phenomena, such as heat friction accumulation, physical adsorption, wear rate, and
703 surface, as well as external conditions.[55] Even though the underlying mechanisms were not
704 defined, the electrostatic charging due to the abrasion and the subsequent heat production was
705 observed in the neat PA6 particles, resulting in lower particle concentration. Focusing on the
706 SMPS results only background signal was observed up to ~400 nm, which was followed by an
707 increase in particles concentration at approximately 700 nm (detection limit of the instrument),
708 indicating the existence of particles in larger dimensions, in accordance with the APS results (SI
709 7).

710 Detection of endotoxin content in PA6, PA6-rGO and rGO

747 An important aspect that needs to be evaluated before any biological assessment of a
748 (nano)biomaterial is the possible contamination by endotoxins. It has been shown that endotoxin
749 contamination of carbon-based nanomaterials may generate artifacts, which could distort
750 biological outcomes, when investigating effects on immune-competent cells.[56] According to the
751 chromogenic endotoxin assay, the endotoxin content in the tested materials was negligible (below
752 0.10 EU/mL). Since it has been reported that GRMs may interfere with traditional endotoxin
753 assays, we further evaluated endotoxin, using the tumor necrosis factor α (TNF α) expression
754 test (TET).[57] As shown in SI 8, none of the materials (PA6, PA6-rGO and rGO) triggered tumor
755 necrosis factor alpha (TNF-α) secretion in human monocyte-derived macrophages (HDMD) in the

756 presence or absence of the specific lipopolysaccharide (LPS) inhibitor, polymyxin B, indicating
757 that our tested materials were endotoxin-free.

Qualitative detection of rGO released from the PA6 matrix

759 It has been shown that fillers such as GRMs may be released from the polymer composite matrix
760 as a result of the matrix degradation (*e.g.,* thermal degradation, hydrolysis, UV exposure), during
761 the routine use of GRM enriched composites.[30,58] The released particles can either be GRMs fully
762 embedded, partially protruding, or completely released (free-standing) from the polymer matrix.
763 Hence, depending on their aerodynamic size and shape, they may pose a threat to human health.

764 Previous studies have shown that the release of fillers from polymer composites could be related
765 to intrinsic failure mechanism. Release of rGO either as protruding or as free-standing from the
766 PA6-rGO composite, during the abrasion process, could be explained by an interfacial debonding
767 between the rGO and PA6 molecules or an adhesive failure as a result of the weak interaction
768 between the rGO and PA6 matrix, as reported by previous studies.[59–62] In addition, failure of
769 graphene sheets is also highly possible, *i.e.,* graphene layer breakage. The failure mechanism of
770 PA6-rGO composites can be examined by visualizing the surface of fractured composites by SEM
771 imaging.[60] The fractured surface of PA6-rGO composites showed rougher structure and deeper
772 cracks compared to that of neat PA6, since the incorporation of rGO could affect the crack
773 propagation of the PA6 composite (SI 9a). Moreover, the characteristic layered and platelet-like
774 structure of rGO was observed as it is released from the PA6 matrix, due to the adhesion failure
775 between rGO and the matrix. Indeed, the exposed rGOs suggested a weak interaction between the
776 rGO and the PA6 matrix, which could also be implied when the composites undergo an abrasion
777 process. In addition, high-resolution TEM analysis of the abraded particles from PA6-rGO
778 composites revealed the layered structure of rGO, appearing as protruding part from the PA6
779 matrix (SI 9b), thus confirming that rGO can be released from the polymer during the abrasion
780 process. It is worth mentioning, that this layered structure can only be observed when rGO is
781 wrinkled or when observed from the side of the stacked layers. Although we observed signs of
782 possible rGO release, it was not possible to draw conclusions on the quantity of rGO released from
783 the polymer. Considering the low percentage of rGO (2.5%) in the PA6 composite and the
784 sensitivity of PA6 polymer even in mild acid conditions, it is technically very complex/impossible
785 to determine the amount of rGO that would be present at the surface of the abraded particles of
786 PA6-rGO or totally released from the polymer matrix.

Impact on lung cells *in vitro*

788 Numerous studies have proven that among the different routes of engineered nanomaterial (NM)
789 exposure, the pulmonary exposure and consequently the respiratory tract is of the highest
790 concern.[11,34,63] Once inhaled, carbon-based materials can reach the deepest regions of the
791 respiratory tract (alveolar region) where they can accumulate for months and distribute to other
792 organs.[64,65] Upon inhalation, respirable particles deposit mainly in the alveolar lung region.[34,66]
793 Potential effects were therefore evaluated in this part of the respiratory tract, using the A549 cell

line (human adenocarcinoma derived-alveolar epithelial type II cells), which is the most commonly applied cell culture model of human alveolar lung epithelium for hazard assessment. In most studies A549 cells are grown in 2D conformation and submerged in cell culture medium, which is not representative of the conditions in the human lung. However, when growing on permeable supports, A549 cells are able to form a polarized tight monolayer and can be maintained at air-liquid interface (ALI) conditions, comparatively resembling native alveolar epithelia.[67,68] In addition, when cultured 24 h at ALI conditions, A549 cells actively secrete surfactant proteins, resulting in a surface tension similar to values measured *in vivo*, in pulmonary alveoli.[69,70] Taking into consideration these important features, A549 cells were selected to assess the biological effects of pristine rGO, abraded PA6 and PA6-rGO composite materials on the alveolar epithelium. Material exposures were performed using a pseudo-ALI approach (where a thin layer of material suspension is applied apically on the insert), without disturbing the surfactant production. Furthermore, pseudo-ALI exposures are more relevant than fully submerged conditions since they result in faster particle deposition, lower particle agglomeration, and higher particle-cell interactions.[68,71,72]

An important consideration when performing safety assessment studies is the use of realistic exposure concentrations. In case of GRMs, human realistic exposure concentrations can only be estimated from the existing limits for CNT pulmonary exposure, where a full working life-time exposure would result in an alveolar mass retention of 10–50 $\mu g/cm^2$ and an acute lung exposure (24 h-48 h) would be in the range of 1 $\mu g/cm^2$.[73,74] The tested doses (2.5–40 $\mu g/mL$) in the present study correspond to 1.3–44 $\mu g/cm^2$ in the different plate formats used for the different cell types and therefore cover the human realistic doses (from low (2.5 $\mu g/mL$) to slightly overload (40 $\mu g/mL$) doses). The selected dose-range is based on human inhalation exposures as it is considered the primary and riskiest exposure route for nanomaterials. Considering other exposure routes (*e.g.* dermal, ingestion exposure) no human exposure data are available. For that reason and for comparability purposes, the same dose range was applied in the different biological systems under investigation.

To determine the acute impact (24 h and 48 h post-exposure) of the materials under investigation on the alveolar cells, cell viability, alterations in morphology and induction of pro-inflammatory reactions were evaluated, at different concentrations of materials (2.5-40 $\mu g/mL$). Adverse effects of particles released from the abrasion wheel on the cell culture models were not anticipated as the quantified amount of released particles was negligible. Moreover, no effects were noted in previous studies using a similar experimental setup.[62,75]

Acute 24 h exposures to either pristine rGO or abraded PA6 and PA6-rGO composite particles did not significantly alter the mitochondrial activity of alveolar epithelial cells at pseudo-ALI conditions, as shown by the MTS viability results (Figure 3a). Similarly, no reduction in cell viability was detected in the alveolar barrier, following 48 h exposure to the tested materials. In accordance with the viability results, no signs of morphological alterations were observed in cells exposed to the highest concentration of abraded particles and rGO (40 $\mu g/mL$) for 48 h, when

compared to the negative control cultures (Figure 3b). Importantly, the alveolar epithelial cell layer was maintained, without ruptures or signs of apoptosis (*i.e.*, fragmented cell nuclei or cellular blebbing) to the nuclei and cytoskeleton.

Analysis of interleukin-8 (IL-8), a critical airway epithelial-derived pro-inflammatory chemokine primarily implicated in acute inflammation and accumulation of neutrophils in inflammatory diseases, revealed that both abraded materials did not induce any effect on IL-8 secreted levels even after 48 h of exposure (Figure 3c).[76] In addition, interleukin-6 (IL-6) a key inflammatory marker (in both acute and chronic inflammation) pivotal for the pathogenesis and exacerbation of numerous pulmonary diseases was evaluated.[77] Exposure to different concentrations of abraded PA6 and PA6-rGO composite materials for up to 48 h did not elicit an increase in IL-6 levels compared to untreated cultures. Since IL-6 and IL-8 are fundamental for the initiation and activation of pivotal inflammatory pathways, evaluation of the secretion of these cytokines provides a valid indication of possible pro-inflammatory reactions. The absence of significant pro-inflammatory responses is in agreement with Wohlleben *et al.* who did not observe any significant toxicity in lung tissue exposed to polyurethane/3% CNT composites.[78] Consistent with our results, Irfan *et al.*, demonstrated that dust particles released from silicon-PA6 composites and neat PA6 composites after a crash and drilling process, did not exhibit significant cytotoxicity following 48 h of submerged exposure in non-polarized A549 cells.[44] Similar observations were also reported in another study where no signs of acute adverse effects (*e.g.,* reduction in mitochondrial activity, or increased secretion of pro-inflammatory mediators) were detected in A549 cells, from neat epoxy or from the addition of CNTs (1%) to the epoxy matrix.[75]

The reliability and sensitivity of the pseudo-ALI A549 model was validated using crystalline quartz (DQ). DQ is a well-known inflammogenic material, classified as a group 1 human carcinogen.[79–81] Several studies reported significant inflammatory effects both *in vitro* and *in vivo* after DQ administration.[70,82–86] Hence, it is frequently used as a positive control for inflammatory responses in hazard assessment studies. As shown in SI 10, 24 h exposure to DQ (100 μg/mL) elicited significant release of both IL-6 and IL-8 in A549 cells, thus further confirming the responsiveness of the A549 cells under the specific culture and exposure conditions.

Similar to the abrasion materials, rGO-exposed A549 cells for 24 h and 48 h did not show evidence of increased pro-inflammatory response, neither in IL-8 nor in IL-6 secretion (Figure 3c). On the contrary, Reshma *et al.,* demonstrated that rGO treatment for 24 h resulted in a dose-dependent reduction in cell viability and NF-κB mediated inflammatory response in A549 2D cultures.[87] Dose-dependent toxicity in rGO exposed BEAS-2B (bronchial epithelial) and A549 (alveolar epithelial) cells was also noted by Mittal *et al.*[19] These differences in biological response could be ascribed to differences in the physicochemical properties of the tested materials as well as differences in cell culture conditions and pseudo-ALI *versus* submerged conditions.
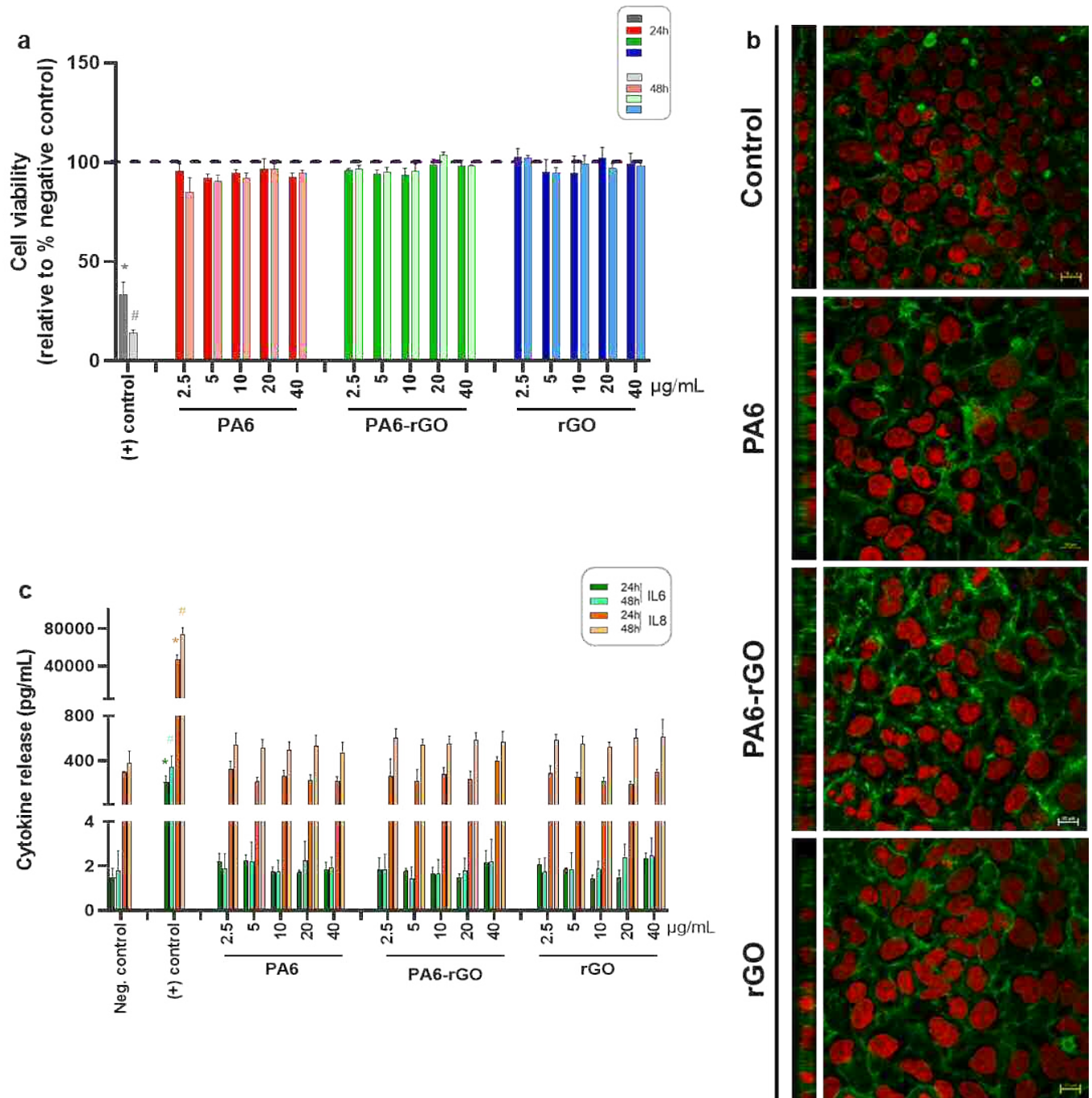
Figure 3. (a) Cell viability of A549 epithelial cells, measured by the MTS assay after 24 h and 48 h treatment with rGO and the abraded particles from neat PA6 and PA6-rGO composites. 1000 μM $CdSO_4$ was used as a positive control. (b) Confocal LSM images of A549 cells after exposure to the tested materials (scale bars: 10 μm). The green color shows F-actin (cytoskeleton), red color shows DNA (cell nuclei). (c) Pro-inflammatory response of A549 epithelial cells after treatment with the tested materials. Concentrations of IL-6 and IL-8 were measured after 24 h and 48 h of materials exposure. One μg/mL TNF-α was used as the positive control. The results are shown as mean ± standard error of the mean (SEM) from at least three independent experiments. * indicates statistical significance compared to the negative control at 24 h of exposure ($p < 0.05$). # shows a statistically significant response ($p < 0.05$) at 48 h of material exposure.

Impact on gastrointestinal cells *in vitro*

Another important exposure route for NMs is through the GI tract, where NMs can either directly be ingested or indirectly enter the GI tract by oral breathing and during the clearance process of formerly inhaled airborne NMs.[88] In contrast to large number of studies focusing on GRM inhalation, the impact of GRMs on the GI system has been largely overlooked, despite the potential implications on human health in both consumer and occupational settings.[89] Caco-2 cells, a human colon adenocarcinoma-derived cell line, is the gold-standard for *in vitro* studies of the human intestinal epithelium, with wide-spread application in pharmaceutical and toxicological research.[23,90] The existing *in vitro* studies have predominantly been performed with non-polarized undifferentiated Caco-2 cells (representing pre-enterocytes) for fast and high-throughput screening of potential substances. Nevertheless, differentiated Caco-2 cells (21 days cultivation on microporous inserts) represent a more reliable model to mimic the small intestine's enterocyte barrier as they more realistically reflect the mature human enterocytes, both morphologically and functionally (*e.g.,* tight and polarized enterocyte-like epithelial cell layers with brush border and tight junction formation).[90–92] Therefore, a toxicological assessment of pristine rGO and abraded PA6 and PA6-rGO, using pseudo-ALI approach to induce the physiologically relevant, fully differentiated Caco-2 cells *in vitro* model of the human small intestinal epithelial barrier was performed.

To evaluate the effects of the tested materials on the intestinal cell viability, the mitochondrial activity was assessed after exposure to material concentrations ranging from 0 to 40 μg/mL for 24 h and 48 h. As shown in Figure 4a, the enterocyte epithelial barrier initially demonstrated high resistance to abraded PA6 and PA6-rGO, as well as, to pristine rGO cytotoxicity. More specifically, cell viability at 24 h was unchanged, without significant reduction of mitochondrial activity, regardless of materials or concentrations tested. At the 48 h time-point, PA6-treated cells remained unaffected, while a slight reduction of viability was reported in PA6-rGO cultures at high concentrations (non-significant $p>0.05$, 20 μg/mL; 77% viability, 40 μg/mL; 79% viable cells). For rGO, the decline in cell viability was more pronounced even at lower material concentrations (10 μg/mL; 72% viability, significant $p<0.05$, 82% and 66% viability at 20 and 40 μg/mL respectively, non-significant $p>0.05$) at 48 h. As only a few reports are available on the effects of GRMs on human enterocytes *in vitro*, and none of the existing studies have investigated the effects of rGO or GRM-embedded composite materials, a comparison with our *in vitro* intestinal results was limited. Nevertheless, the lack of acute effects on mitochondrial activity even at high concentrations (up to 80 μg/mL) was noted by Kucki *et al*. who investigated the toxicological impact of four types of GOs on undifferentiated Caco-2 cells for 48 h.[23] Similarly, the viability of undifferentiated Caco-2 cells remained unaffected, following exposure to GO and few layer graphene (FLG) repeatedly for 4 days.[93] It is pertinent to note that previous studies reported that NM and, in particular, GRM uptake is significantly lower in differentiated Caco-2 barrier models compared to undifferentiated cells due to the lack of typical structures (*e.g.,*

916 microvilli and tight junctions), which hinder NM internalization.[90,93,94] Hence, despite higher
917 internalization, no acute toxicity GRM effects were noted in the existing studies.

918 To evaluate the functional integrity of the intestinal barrier, the transepithelial electrical resistance
919 (TEER) values before and after material exposure were measured. No significant TEER reduction
920 was reported when differentiated Caco-2 cells, were exposed to abraded PA6 or PA6-rGO even
921 after 48 h of exposure (Figure 4b). Similarly, no effect on barrier integrity was observed following
922 exposure to pristine rGO, suggesting that the observed loss in mitochondrial activity did not have
923 any impact on the barrier function. Consistent with our results, Domenech *et al.* found that neither
924 GO nor graphene nanoplatelets (GNP) exposures were able to affect the functional/structural
925 integrity of an intestinal co-culture barrier model (Caco-2/HT-29 cells), as reported by TEER and
926 permeability measurements.[91] In addition, membrane integrity of cells was maintained even after
927 treatment with digested GOs in a Caco-2 undifferentiated monolayer and a triple co-culture (Caco-
928 2/HT-29/Raji) intestinal model.[93,95]

929

930 The lipid absorption at the brush borders of the enterocytes is a fundamental physiological function
931 of the intestinal barrier.[96] To investigate possible alterations in the fatty acid uptake of
932 differentiated Caco-2 cells after treatment with abraded composite materials and rGO, a lipid
933 uptake assay was performed. Cell treatment with fatty acid synthase inhibitor C75 resulted in a
934 significant decrease in lipid uptake at both 24 h and 48 h (Figure 4c), suggesting a major defect in
935 lipid absorption, in agreement with the observations of Hempt *et al.*, and Accioly *et al.*[97,98] On the
936 contrary, no significant changes in fatty acid absorption were detected after treatment with abraded
937 PA6, PA6-rGO and pristine rGO for 24 h. At 48 h of treatment with abraded PA6 and PA6-rGO a
938 significant reduction was only observed at the concentration of 10 μg/mL (79% and 75%
939 respectively, $p<0.05$), however the higher material concentrations did not induce any evident effect
940 in lipid uptake. In the case of rGO, a notable loss of fatty acid uptake was shown at the highest
941 concentration tested, following 48 h of exposure (40 μg/mL; 64%, $p>0.05$). It should be
942 emphasized that no previous studies have analyzed possible alterations in the lipid absorption
943 function of the intestinal barrier after GRM or other carbon-based material exposure. Interestingly,
944 a previous study using synthetic amorphous silica did not observe any decline in the lipid uptake
945 in a triple intestinal culture (Caco-2/HT-29/Raji co-culture) after 48 h of exposure.[97]
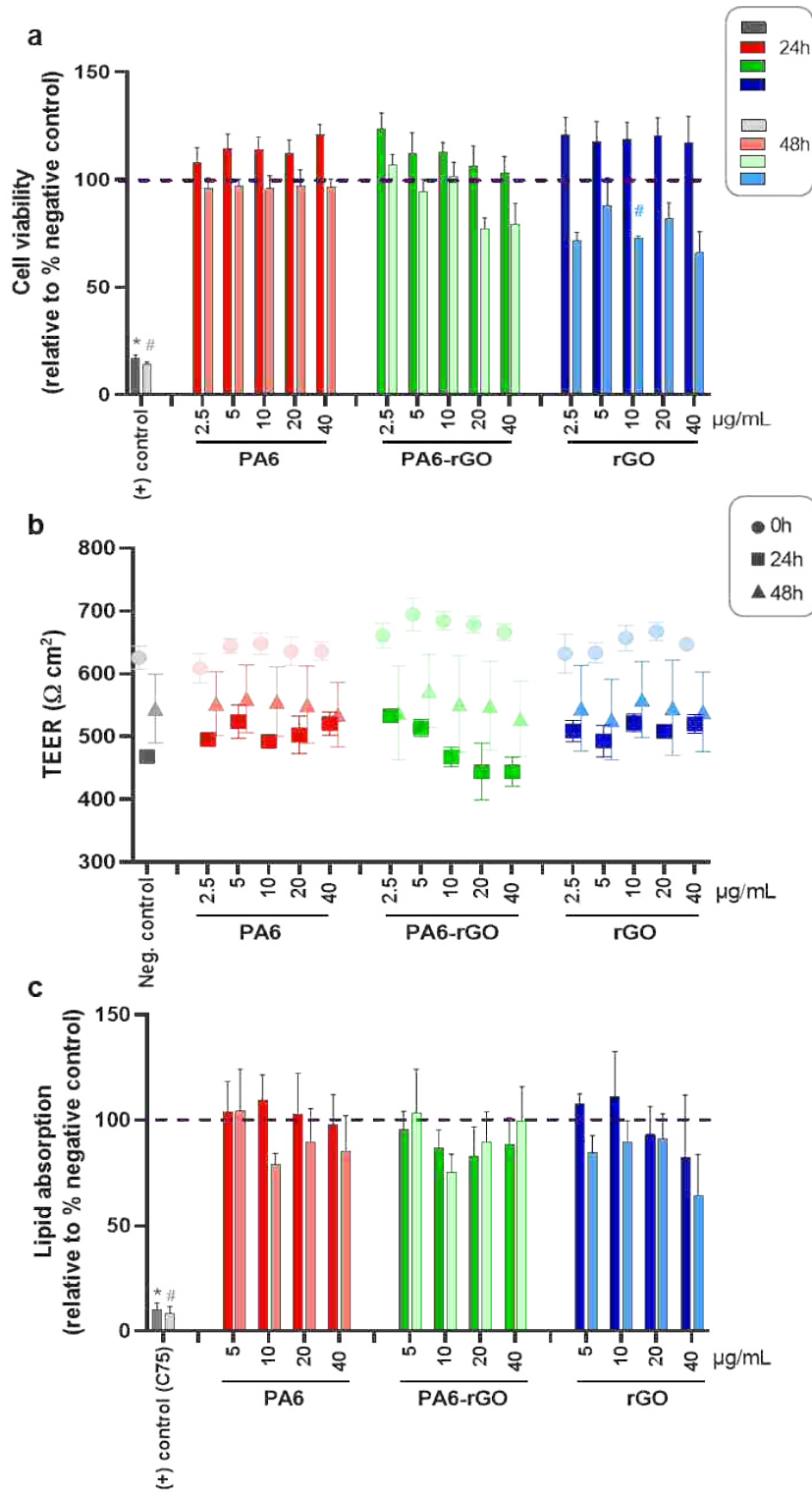
Figure 4. (a) Impact of abraded particles (PA6, PA6-rGO) and rGO on cell viability of differentiated CaCo-2 intestinal epithelial cells after 24 h and 48 h of exposure (MTS assay). $CdSO_4$ served as a chemical positive control. (b) Assessment of the barrier integrity by TEER measurement before and after exposure to the tested materials (c) Lipid absorption was determined following 24 h and 48 h of exposure to the tested materials. Treatment of cells with the fatty acid synthase inhibitor C75 (50 µg/mL) for 24 h served as a chemical positive control for the investigation of lipid uptake. The results are shown as mean ± SEM from at least three independent experiments. * indicates statistical significance compared to the negative control at 24 h of exposure ($p < 0.05$). # shows a statistically significant response ($p < 0.05$) at 48 h of material exposure.

Impact on skin cells *in vitro*

The skin as the largest organ in the human body, with primary functions to defend and maintain physiological conditions, is considered one of the most common routes for GRM exposure, during the life cycle of GRM containing products.[35,99,100] Epidermal cells consist mainly of keratinocytes, structurally involved in maintaining the barrier function of the epidermis, but also exerting a key role in the initiation and perpetuation of skin inflammatory and immunological responses at the skin level.[101] Therefore, the potential dermatoxic effects of abraded rGO-composite materials and pristine rGO were investigated on human HaCaT skin keratinocytes, a non-tumorigenic, spontaneously immortalized human keratinocyte cell line, already employed to study skin toxicity of pristine GRMs.[102–105]

Initially, the acute effects on cell viability were evaluated by means of mitochondrial activity of HaCaT cells after two exposure times (24 h and 48 h) by the MTS assay (Figure 5a). The pristine rGO induced a significant reduction of cell viability only after 48 h exposure to the highest concentration (40 µg/mL; 78% cell viability, $p < 0.05$), in line with the weak cytotoxic effects induced by other pristine GRMs such as FLG and GO on the same cell type.[104] However, treatment of keratinocytes with abraded particles from neat or rGO-reinforced PA6 composites did not induce any decrease in mitochondrial activity. In contrast, a slight increase on cell viability was observed after 24 h exposure, which was more pronounced after 48 h exposure (significant from the concentration of 5 µg/mL, $p < 0.01$). In particular, after 48 h, abraded PA6 and PA6-rGO particles increased cell viability at 143% and 148%, respectively, at the highest concentration. To further validate the results from the MTS assay, the WST-8 assay was also performed, as a widely used assay to evaluate the mitochondrial damage caused by different GRMs on a wide range of *in vitro* models, including HaCaT keratinocytes.[102,104,106,107] WST-8 confirmed the results obtained by the MTS, although more substantial effects were reported (Figure 5b). More specifically, rGO induced a significant reduction of cell viability after 48 h exposure to the highest rGO concentration (40 µg/mL; 64% cell viability, $p < 0.001$). Moreover, as observed with the MTS assay, abraded PA6 and PA6-rGO particles significantly increased cell viability, already after 24 h exposure and starting from the concentration of 10 µg/mL (142% cell viability, $p < 0.05$) for PA6 and at the highest concentration of 40 µg/mL PA6-rGO (156% cell viability, $p < 0.05$). The effect was more pronounced after 48 h exposure, being significant starting from the concentration of 5 µg/mL ($p < 0.05$), inducing a maximum increase of 167% and 173% for abraded PA6 and PA6-rGO particles, respectively, at the highest concentration. To quantify the viable attached cells, without relying on metabolic activity measurements that might lead to false positive overestimation of cell viability, the cell mass was determined using the well-established SRB assay.[108] A similar trend to the mitochondrial activity assays was observed. Pristine rGO resulted in a slight but significant reduction of cell mass at 40 µg/mL (90%, $p < 0.05$), while abraded composite particles significantly increased cell mass (113%, $p < 0.05$, and 117%, $p < 0.05$, for PA6 and PA6-rGO, respectively) at the same concentration, and after 48 h of exposure (Figure 5c). To further investigate whether abraded PA6 can promote cell proliferation, the % of

proliferating cells was determined as shown in Figure 5d. No alteration of cell proliferation was induced by exposure to pristine rGO for neither 24 h nor 48 h. On the contrary, abraded PA6-rGO and PA6 increased cell proliferation already after 24 h at the highest concentrations ($p < 0.05$). At 48 h of exposure to abraded composites, cell proliferation was more evident, being significant already at the concentration of 10 μg/mL and inducing maximum effects of 147% and 144% for abraded PA6 and PA6-rGO, respectively ($p < 0.05$). These results suggest that: *i*) the increased cell viability induced by abraded PA6 and PA6-rGO may be dependent on a proliferative stimulus and *ii*) the proliferative stimulus seems to be exerted by abraded PA6. Indeed, Dias *et al.* recently reported the ability of PA6 to promote cell proliferation in murine fibroblasts when employed as a nanostructured scaffold, indicating its potential of modulating skin regeneration and wound healing parameters at cellular and histological levels.[109] This phenomenon may be explained by the structural similarities between PA6 and proteins. Indeed, the amide groups of the polymer can interact by hydrogen bonds with cellular molecules, providing a structural environment able to improve cell growth.[109] In addition, cell proliferation may be promoted and sustained by the hydrophilic wetting behavior of PA6.[110]

Possible alterations in cell morphology were visualized by confocal microscopy after staining plasma membranes of HaCaT cells with the DiL fluorescence dye. Negative control cultures displayed the typical cobblestone morphology of skin keratinocytes, which was slightly condensed in cells treated with 40 μg/mL of each material for 48 h, particularly for rGO-treated cultures. Moreover, the morphology of rGO-treated cells showed a moderate cell shrinkage, in line with the observed cytotoxic effect.

Fusco *et al.* recently reported that keratinocytes are able to selectively sense and interact with GRMs at amounts as low as 1 μg/mL.[111] In addition, further analysis reported that GRM cytotoxic effects on HaCaT cells are only partially reversible, probably because of their ability to be internalized inside keratinocytes.[102] To investigate the interactions between the materials and epidermal cells, HaCaT cells exposed to pristine rGO, abraded PA6-rGO and PA6 (40 μg/mL) for 48 h were subjected to confocal microscopy analysis, in which materials were visualized in white exploiting their light reflection properties during the confocal acquisition. As shown in Figure 5e, rGO and PA6-rGO were able to interact with cells, where the presence of rGO, and to a far less extent PA6-rGO, was visualized bound to the membranes and inside keratinocytes. In line with this observation, using reflection mode acquisition, different GRMs (*e.g.* GO, FLG) were captured to interact and penetrate the plasma membrane of HaCat cells.[104] Reflection mode, however did not allow the detection of the abraded PA6 polymer in the cells, due to low contrast of these particles. Similarly, the low signal given by PA6-rGO acquired in reflection mode by confocal microscopy analysis could be ascribed to a quenching effect by PA6 polymer bound to rGO. This hypothesis is supported by the lack of light reflection properties of PA6, which could partially mask the signal given by rGO.
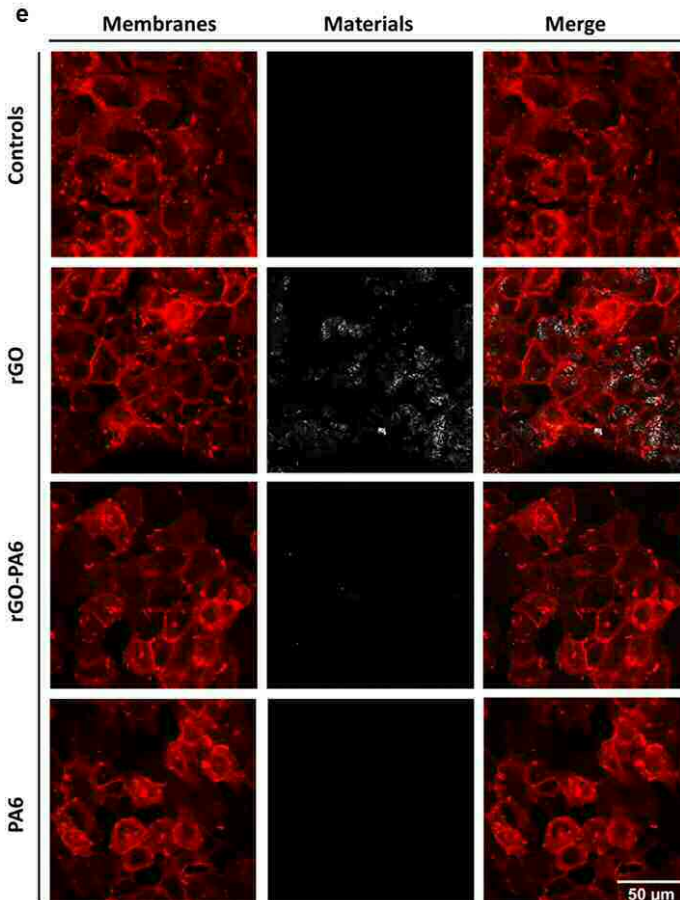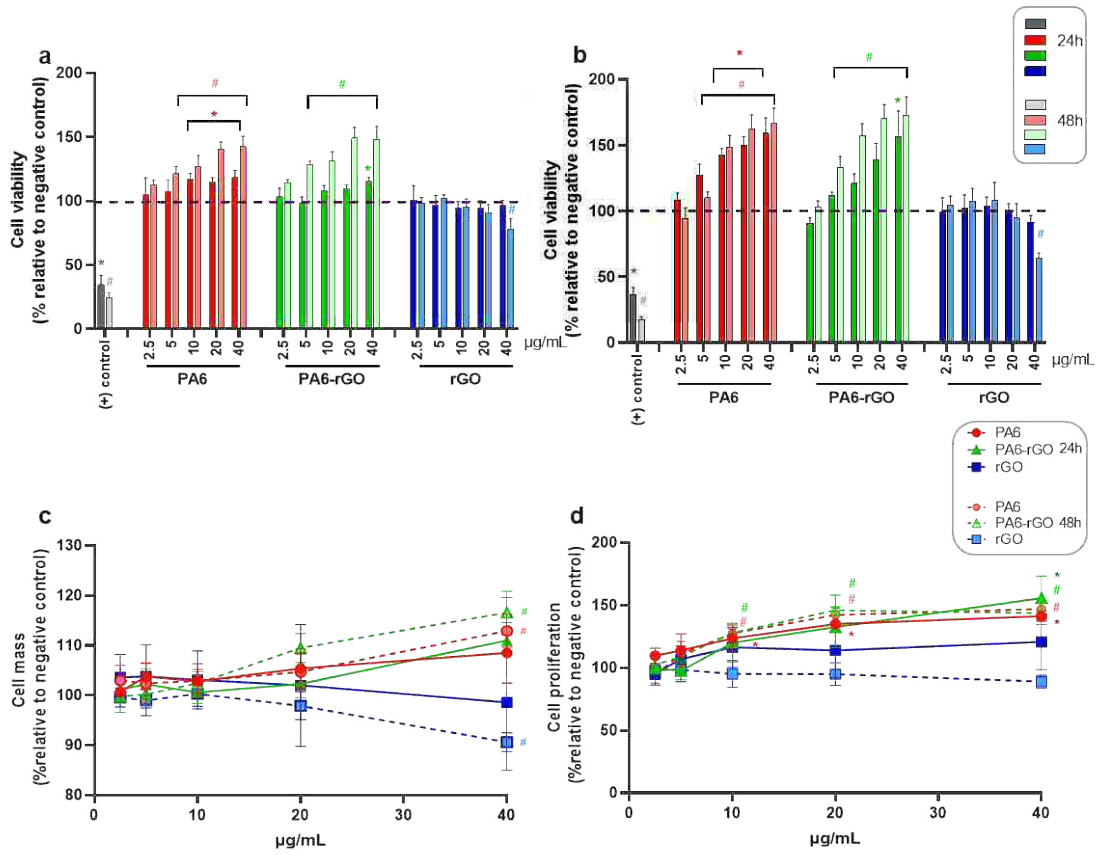
Figure 5. Effect of rGO and abraded PA6 and PA6-rGO on the mitochondrial activity of HaCaT cells evaluated by (a) the MTS assay and (b) the WST-8 assay. Potential effects of the tested materials on skin cell proliferation assessed by (c) the SRB incorporation assay and (d) the BrdU assay. Data are the mean ± SEM of 3 independent experiments. * indicates statistical significance compared to the negative control at 24 h of exposure ($p < 0.05$). # shows a statistically significant response ($p < 0.05$) at 48 h of material exposure. (e) Confocal micrographs of HaCaT cells exposed to 40 µg/mL of rGO, abraded PA6-rGO and abraded neat PA6 for 48 h. Plasma membrane of HaCaT cells was labeled with the fluorescence DiL dye (red, left panel). rGO is visualized by reflection mode acquisition (white, middle panel); confocal reconstruction of red DiL labeled HaCaT cells merged with white reflecting rGO (merged images, right panel). Original magnification: 60×. Scale bar: 50 µm.

Impact on immune cells *in vitro*

The immune system identifies and protects the body from infections and other exogenous materials. Therefore, understanding the interaction of GRMs with the pivotal cells of the innate immune system is of particular importance.[112–115] The key front-line cells of the immune system assigned to eliminate foreign materials and assist in tissue remodeling after injury across the whole body are macrophages.[116] In a pulmonary exposure scenario, macrophages will be the first immune cells interacting with GRMs and dealing with their clearance or long-term persistence.[50,66,117,118] The effect of abraded particles and pristine rGO was therefore assessed in human macrophage differentiated THP-1 cells. The biological response was also tested in murine macrophage-like cells (RAW 264.7) to determine possible difference in the behavior of the tested materials towards human or murine cells. THP-1 and RAW 264.7 macrophage models act as proxy for either tissue-recruited macrophages upon inflammation signaling or tissue resident macrophages, such as alveolar macrophages in the lungs.

Cell viability of THP-1 differentiated and RAW 264.7 macrophages exposed to PA6, PA6-rGO and rGO was determined using the MTS assay. As seen in Figure 6 a-b, abraded PA6 and PA6-rGO did not decrease the mitochondrial activity of either THP-1 differentiated or RAW 264.7 macrophages even at the highest concentration (40 µg/mL). In agreement with our findings, Netkueakul *et al.* did not observe any significant cytotoxic effects of abraded particles from epoxy/1%GRM (GOs, rGO or GNPs) composites on THP-1 differentiated macrophages, at the same exposure concentrations.[62] In the same study, pristine GRMs, including rGO, did not reduce the cellular mitochondrial activity upon exposure to concentrations of up to 40 µg/mL. In addition, studies focusing on abraded polymer composites reinforced with other carbon-based materials, *i.e.,* CNTs, found that the abraded particles from epoxy/1%CNT composites did not cause acute effects on mitochondrial activity of THP-1 cells, while pure CNTs resulted in a significant decrease in cell viability.[75] In accordance with the above reported cell viability results in the skin and GI *in vitro* models, pristine rGO did induce a dose-dependent loss of cell viability in both macrophage cell lines (significant at concentrations of 20-40 µg/mL for THP-1 cells and 10-40 µg/mL for RAW 264.7 cells, respectively). Moreover, no induction of cytotoxic reactions was reported for RAW 264.7 macrophages after exposure to abraded materials, while a significant release of lactate dehydrogenase (LDH) was observed, following 24 h exposure to 20 and 40 µg/mL of pristine rGO, supporting the MTS data (SI 11). Consistent with our results a dose-dependent decline in cell viability, especially at higher rGO concentrations (from 20 µg/mL), has been observed in bone marrow derived macrophages as well as in the J774A.1 macrophage cell line.[119] This stands in

contrast with the work of Netkueakul *et al*. and Li *et al*. where no significant cytotoxicity was shown in rGO-treated THP-1 cells.[21,62] Those differences in biological responses may depend on differences in the lateral dimensions, thickness and the amphiphilic properties of the materials.

Macrophages are also known to be involved in the initiation, progression, and resolution of inflammation.[120] Hence, to further evaluate the immunological impact of the tested materials in differentiated THP-1 cells, a multiplex-cytokine array analysis of ten crucial pro-inflammatory mediators was conducted at a sub-toxic concentration (20 μg/mL). In parallel, hierarchical clustering was carried out to draw associations between cytokine responses evidenced for pristine rGO, the abraded PA6-rGO and PA-6, the LPS positive control, *versus* the negative control in human macrophages (Figure 6e). The cytokine profiling analysis clearly demonstrated that the effects induced by the tested materials are distinctly different from the effects of LPS. Moreover, the cluster analysis suggested that the cytokines could be broadly separated into two main clusters: those affected by high secretion of cytokines generated by the LPS treatment and those affected by rGO, PA-6-rGO, and PA-6 treatment. More specifically, a significant increase in the secretion of interferon gamma (IFN-γ) was revealed in THP-1 cells when exposed to rGO and PA-6, comparable to the effect induced by the positive control LPS, a well-known stimulator for cytokine secretion in these cells. Moreover, two classical Th1 pro-inflammatory cytokines, TNF-α and interleukin-1beta (IL-1β), were significantly upregulated following acute exposure to all three materials (SI 12a), and IL-1β production was blocked by the pan-caspase inhibitor, zVAD-fmk and the selective NLRP3 inhibitor, MCC950 (SI 12b), suggesting that these materials triggered inflammasome activation, as shown for several other NMs.[121] No significant release of IL-2, IL-4, IL-6, IL-8, IL-10, IL-12 and IL-13 was reported in material-treated THP-1 cells compared to the untreated cells. Similar to the results obtained with human macrophages, murine RAW 264.7 cells did not show significant upregulation of the crucial cytokine IL-6 regardless of the material applied, while significant TNF-α release was noted following exposure to all three materials (20 and 40 μg/mL for PA6 and PA6-rGO, all tested concentrations for rGO), as shown in Figure 6d. Comparing THP1 and RAW 264.7 cells, no species-to-species variations in the investigated biological responses were observed, as similar effects were reported in both human and mouse cells.
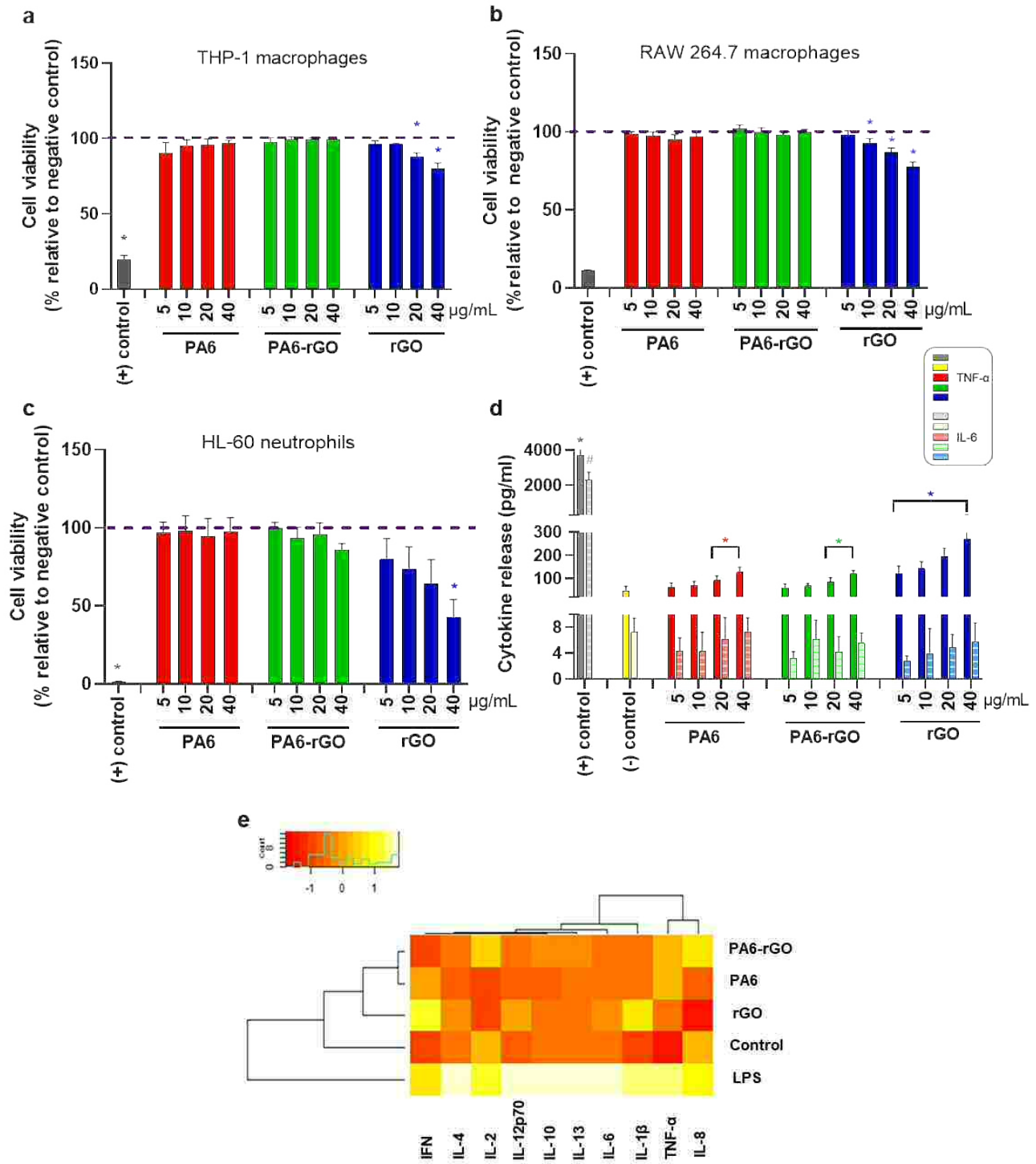
1121

Figure 6. Cell viability (MTS assay) of (a) THP-1 and (b) RAW 264.7 macrophages and (c) neutrophil-like HL-60 cells (ATP assay) exposed to increasing concentrations of rGO and abraded PA6 and PA6-rGO composites for 24 h. (d) Cytokine release by RAW264.7 macrophages. IL6 and TNF-α levels were determined after incubation with

1125 increasing concentrations of PA6, PA6-rGO and rGO. Cells exposed to 1 µg/mL LPS were used as positive control.
1126 Data are the mean ± SEM of 3 independent experiments. The * symbol represents $p<0.05$ as compared to the negative
1127 control. (e) Cytokine profiling and hierarchical cluster analysis of inflammatory mediators released in differentiated
1128 THP-1 macrophages exposed to rGO, abraded PA6-rGO and PA6. Cells exposed to 0.1 µg/mL LPS were used as
1129 positive control. Each branch in the dendrograms shows the similarity between samples; the shorter the branch, the
1130 more similar the samples.

1131 Previous reports showed that neat polymer matrix materials such as epoxy did not trigger
1132 significant pro-inflammatory responses on immune cells.[62,75] However, the present study
1133 demonstrated that abraded neat polymer PA6 did elicit significant release of three pivotal pro-
1134 inflammatory proteins in THP-1 cells. More specifically, upregulation of IFN-γ, a key player in
1135 host-defense against pathogens, might indicate that abraded particles from this polymer matrix
1136 may be recognized as intracellular parasites by THP-1 cells, leading to increased IFN-γ
1137 secretion.[122] Moreover, both abraded materials (neat polymer PA6 and composite PA6-rGO)
1138 resulted in secretion of TNF-α and IL-1β cytokines that would typically lead to recruiting more
1139 immune cells *i.e.*, neutrophils, monocytes/macrophages to the affected areas, as a hallmark of acute
1140 inflammation.[123] In addition to the endogenous inflammogenic potential of the polymer matrix,
1141 the potential inflammation of PA6-rGO could be explained by the transformation of rGO during
1142 the production process of the composite or due to protruding or released GRMs from the polymer
1143 matrix. However, the magnitude of the pro-inflammatory effect induced by the abraded PA6-rGO
1144 particles was notably lower compared to that induced by pristine rGO or the LPS control,
1145 suggesting only a minor pro-inflammatory response (SI 7b). Since the PA6-rGO composite
1146 material contains only a small percentage of rGO (2.5%), the observed limited toxicity of the
1147 composite material (containing a small % of rGO) compared to the pristine rGO is probably due
1148 to the low amount of rGO in the composite, the endogenous inflammogenicity of the neat polymer
1149 PA6, and not to a different mechanism of toxicity. Previous studies showed that GRM (particularly
1150 GO) treatment could provoke inflammatory responses, including the production of inflammatory
1151 cytokines by macrophages.[115,122,123] The cytokine profiling experiments revealed that rGO
1152 triggered the cytokine production of the M1 markers TNF-α and IL-1β in THP-1 cells, suggesting
1153 possible inflammasome activation. These findings support those recently reported by Gurunathan
1154 *et al.* who observed significant stimulation of TNF-α and IL-1β secretion, following exposure to
1155 vanillin-functionalized rGO in THP-1 cells.[124] A similar trend was found for TNF-α secretion in
1156 primary and J774A.1 macrophages after treatment with two types of rGO.[119]

1172 To gain more insights into the interaction of the tested materials with macrophages, the cellular
1173 morphology was closely examined. Conventional light microscopy images of RAW 264.7
1174 macrophages upon 24 h exposure to abraded PA6 and PA6-rGO materials revealed no signs of
1175 modification in cellular morphology even at the highest concentration of 40 µg/mL (SI 13).
1176 Correspondingly, no major alterations were observed in THP-1 cells after 24 h exposure to abraded
1177 GRM epoxy composites.[62] In the case of pristine rGO, although increased rGO accumulation was
1178 observed on the cells surface, the shape of the RAW264.7 macrophages was not affected at low
1179 concentrations (5-20 µg/mL). However, macrophages treated with 40 µg/mL of pristine rGO
1180 showed a rounder appearance compared to untreated control cells. In good agreement with our

1181 observations a loss of protrusions with a subsequent morphological shift towards rounded cells has
1182 been previously demonstrated after rGO exposure (20 µg/mL) in primary macrophages.[119] The
1183 observed morphological alterations might indicate an increased rGO internalization by the
1184 macrophages. Moreover, the significant TNF-α secretion in RAW 264.7 cells could lead to the
1185 activation of macrophages into a pro-inflammatory state, which can lead to similar alterations in
1186 the cellular shape and could be a hint for the intrusion of rGO onto the plasma membrane, as shown
1187 by Wu *et al.*[119] In support to that Li *et al*. demonstrated that while GO nanosheets are mostly
1188 associated with the surface membrane in THP-1 cells, rGO was principally internalized by by
1189 phagocytosis.[21]

1190 Several studies have shown that macrophages may be more susceptible than other cell types to the
1191 biological effects of particles, due to the greater dose of internalized particles. A previous study of
1192 a panel of metal oxide nanoparticles showed that the alveolar macrophage cell line was the most
1193 sensitive cell model among the 12 cell models tested.[125] The toxicity of metal/metal oxide particles
1194 may be explained by the rapid dissolution of the particles in the acidic environment of the
1195 lysosomes. In addition, high aspect ratio materials may cause lysosomal destabilization, and
1196 subsequently lead to pro-inflammatory cell activation. However, the materials tested here are not
1197 considered high aspect ratio materials as abraded particles and GRMs are not necessarily fiber-
1198 like and their biological effects depend on different material properties, not only the lateral
1199 dimensions.[27] Nonetheless, the lateral dimensions of graphene oxide (GO) have been shown to
1200 play a role for interleukin-1β (IL-1β) and transforming growth factor-β1 (TGF-β1) production and
1201 a more recent study has confirmed that the lateral dimensions may impact on cellular uptake and
1202 subsequent biological effects in liver cells. [126,127]

1203 Another important immune cell type often neglected in toxicological studies is neutrophils, the
1204 most abundant circulating leukocytes and among the first cells to be recruited in the airways, upon
1205 lung exposure to GRMs.[128] These cells also play a key role in the initiation of inflammation in
1206 several tissues as well as in GRM biodegradation processes.[129–131] There is a paucity of data on the
1207 biological effect of GRMs on neutrophils and the few available studies mainly focused on the
1208 degradation of GRMs by a myeloperoxidase-dependent mechanism in neutrophils and not on
1209 immunotoxicity. Mukherjee *et al.* recently reported that GO sheets with differing lateral
1210 dimensions triggered a dose-dependent loss of mitochondrial activity in neutrophils as measured
1211 by the ATP assay. At the same time, GO acted directly on the neutrophil cell membrane, leading
1212 to cell activation.[129] Therefore, it is important to know if pristine rGO and abraded particles from
1213 rGO-reinforced composite materials have an impact on neutrophils. Focusing on neutrophils, cell
1214 viability was determined on differentiated HL-60 cells using the ATP assay, as the MTS assay was
1215 not appropriate for this non-adherent cell line (data not shown). Consistent with the macrophage
1216 viability results, no significant effect on the viability of PA6 or PA6-rGO exposed HL-60 cells
1217 was observed (Figure 6c), but a 24 h rGO treatment revealed a dose-dependent loss of
1218 mitochondrial activity, only significant at the highest concentration (40 µg/mL, 50% viability). In
1219 addition to the viability assay, a cytokine array was performed in neutrophils to examine possible

1220 induction of pro-inflammatory processes (SI 14). In contrast to THP-1 cells, cluster analysis in
1221 exposed HL-60 cells revealed a large single cluster with low cytokine secretion for all tested
1222 cytokines, suggesting that neutrophils might not be a good model for cytokine screening.
1223 Furthermore, in HL-60 cells, no distinct cytokine upregulation was reported, except for LPS-
1224 treated cells (SI 1).

1225 An important, non-trivial matter in relation to the *in vitro* results obtained with respect to pristine
1226 rGO, abraded neat PA6 or rGO-reinforced PA6 is the *in vitro* dosimetry. It has been shown that
1227 cellular uptake of gold nanoparticles depends on their sedimentation and diffusion velocities, while
1228 it is independent of size, shape, density, surface coating and the initial concentration of the
1229 nanoparticles. [132] More recent studies of so-called "bouyant" nanoparticles (*e.g.* polypropylene)
1230 have shown that their biological activities may be underestimated when using conventional
1231 submerged cell culture methods.[133] In the present study, A549 and Caco-2 cells were exposed
1232 using a more physiologically relevant (for the lung and the GI) pseudo-ALI approach, which
1233 allows faster particle sedimentation and more particle-cell interaction compared to the
1234 conventional submerged exposures. Regarding the skin (HaCaT) and immune (THP-1, RAW
1235 264.7, and HL-60) cells, such pseudo-ALI exposures are not relevant; therefore, submerged
1236 exposures were applied. The existing models to estimate *in vitro* concentration of nanomaterials
1237 in submerged conditions (*e.g.* the *in vitro* sedimentation, diffusion, and dosimetry (ISDD) model,
1238 the distorted grid (DG) model, or the 3D-sedimentation-diffusion-dosimetry (3DSDD) model)
1239 were developed and are suitable only for spherical particles, such as spherical silica, gold, and
1240 metal oxide nanoparticles. They have a limited applicability for non-spherical materials (*e.g.*
1241 GRMs and CNTs) due to their different form factor and heterogeneity.[134–136] Consequently,
1242 determining the GRM cell delivered dose in submerged conditions is still a challenge due to the
1243 analytical difficulties of quantifying the GRM dose delivered to cells, as it would require several
1244 analytical techniques and cellular uptake quantification. Particularly, for the abraded PA6 and
1245 PA6-rGO materials, it would be almost impossible as the cellular internalisation cannot be
1246 visualised with the existing methodology *i.e.,* TEM, Raman microscopy or optical microscopy and
1247 LSM reflection mode (as we have shown for RAW 264.7 and HaCaT cells).

1248

Pulmonary effects in mice

1250 The *in vitro* investigations demonstrated that pristine rGO was the material of highest concern
1251 amongst the tested materials, and that the immune cells and in particular the macrophages were
1252 the most responsive *in vitro* models both with respect to abraded materials (neat PA6 and PA6-
1253 RGO) and pristine rGO. Amongst all exposure routes, inhalation is the most rapid route of entry
1254 into the body and the only route in which macrophages would interact immediately, and without
1255 any intervening barrier, with the materials, should these respirable materials reach the alveoli.
1256 Considering that macrophages and neutrophils along with epithelial cells are the key drivers of the
1257 pulmonary response to respirable materials reaching the alveoli, we sought to study whether the

rGO results obtained *in vitro* would translate into a macrophage-driven inflammatory response in the lungs of mice. Based on the *in vitro* results, we anticipated that abraded (neat PA6 and PA6-rGO) materials would cause limited inflammation *in vivo* while the response to pristine rGO would be more pronounced but still moderate. Moreover, the comparative results obtained using epithelial A549 lung cells (negative) and THP-1/RAW264.7/HL-60 immune cells (positive) suggested that the pulmonary response to rGO would be mostly driven by the resident macrophages, but would not prevent the resolution of this inflammation with time.

After a single exposure to abraded PA6-rGO, histopathological analysis of lung sections did not reveal any alteration of the lung tissue at the tested time-points (Figure 7a). Absence of obvious cell recruitment or tissue damages was also noted after exposure to the low dose of pristine rGO (rGO-0.3 µg), neat polymer alone (PA6) or vehicle control. In contrast, exposure to high dose of pristine rGO (rGO-15 µg) induced macrophage-driven granuloma-like formations at all considered time points, and a clear infiltration of immune cells at 1 and 7 days. Interestingly, the location of those inflammatory structures were overlapping with material accumulation sites. Such reactions to foreign materials occur when materials cannot be easily eliminated from the tissue.[137,138] The key component of granuloma-like formation is the fusion of numerous macrophages into multinucleated cells, which are able to phagocytize particles that can be larger than 10 µm.[138] Noteworthely, the pronounced inflammatory structure formation observed at day 1 and 7 was followed by an obvious tissue recovery by day 28 (*i.e.*, with notable reduction in granuloma size, Figure 7a). These results are not consistent with the findings of a previous study in which a prolonged inflammation over 90 day after exposure was associated to the presence of large, black and compact rGO agglomerates that persisted in lung tissue for up to 90 days without being phagocytosed.[118] These results suggest that bio-persistence of materials was the leading cause for a prolonged inflammation, hence material clearence could in contrast be associated to inflammation resolution. In our study, the decrease in granuloma size and resolution of cell influx and inflammation over time is therefore likely to result from a successful rGO internalization and elimination by macrophages. Moroever, the *in vivo* pulmonary impact of rGO has been largely overlooked in comparison to other GRMs.[26] In the few existing studies comparing GO and rGO, GO seemed to provoke more inflammogenic responses compared to rGO.[118,139]

Adverse effects were also assessed by measuring total protein and LDH release to the airways. These two markers are typically used as hallmarks of lung epithelium tissue damage.[140] For the abraded PA6-rGO and PA6 materials, no significant variations of protein concentration or LDH activity in bronchoalveolar lavage (BAL) fluid were observed (Figure 7b-7c), suggesting no disruption of the air-blood barrier and the lung epithelium, in agreement with the absence of responses found in the A549 cell model (Figure 2). Despite the observation of granulomatus formation after exposure to high dose of rGO (rGO-15 µg), no significant ($p>0.05$) effects on BAL proteins or LDH release were seen at 1, 7, or 28 days post-exposure, suggesting that the response to rGO was mostly driven by immune cells.

In BAL fluid, no variation in the total cell number was observed for any of the materials tested (Figure 7d), but there was an increase in neutrophil numbers at day 1 after exposure to either abraded PA6-rGO or PA6 (Figure 7e). Nevertheless, this neutrophil recruitment was not stastistically significant compared to the negative control. In contrast, a significant increase in neutrophils was found after exposure to rGO-15 µg, whereas no difference was observed for the lowest dose (rGO-0.3 µg) compared to the negative control. Interestingly, 7 days after exposure, an increase in eosinophils was found in the alveolar space of mice treated with either PA6-rGO (p=0.1217) or rGO-15 µg (p=0.0543). However, after 28 days, we did not detect any difference in eosinophils or neutrophils compared to the negative control for any of the materials tested. This suggested a recovery from the inflammatory stressor and is in agreement with the histological evaluation. Despite this recovery, the presence of multinucleated macrophages was still significant at 28 days for rGO-15 µg in comparison to the negative control or other conditions, suggesting that the higher amount of materials was delaying clearance and complete resolution.

To further characterize the lung inflammatory response, the concentration of 13 inflammatory mediators was evaluated in digested lungs at days 1, 7 and 28. As shown in Figure 8, there was no significant change in any of the mediators tested, suggesting a low inflammatory profile for all the materials tested. In addition, the concentration of TNF-α and IL-6 was assessed in the BAL fluid and found to be below the detection limit (7.8 pg/mL) of the assay (SI 16). Taken together, neither BAL fluid nor whole lung measurements showed significant cytokine secretion, which is in line with the moderate influx of immune cells in BAL fluids (PMNs, macrophages, or lymphocytes), irrespective of the materials considered (Figure 7e).

It should be noted that the unaligned significant response observed for one animal (out of 3) for all tested cytokines (and total cell number) after exposure to abraded PA6 at 28 days (Figures 7 and 8) was not anticipated. The discrepancy could not be attributed to technical or instrumental errors as the measurements were repeated and obtained the same results. In addition, the health and behaviour of this specific animal before the terminal procedure was not of concern (data not shown); hence, there was no valid reason for removing the animal from the study. The observed odd response should therefore be attributed to animal variability.

In summary, pulmonary exposure to abraded PA6-rGO in mice induced a weak but not significant lung inflammation characterized by a transient influx of neutrophils and eosinophils in the alveolar space. In contrast, a high dose of pristine rGO induced a persistent presence of immune cells in the alveolar space, in particular macrophages associated with the clearance of materials, without affecting the overall resolution of inflammation with time. Importantly, this inflammation in the form of cell recruitment but without cytokine secretion was not associated with any tissue remodelling within the time-frame investigated. Since the administered bolus dose of 15 µg is considered a high dose, representing a worst-case scenario, the limited animal findings underline the likely low toxicity of the tested abraded composites or the pristine rGO, in any realistic exposure scenario. Overall, the *in vivo* results are in good agreement with the *in vitro* biological assessment data, in particular the lung epithelial cells (A549), the macrophages (THP-1 and RAW

264.7) and neutrophils (HL-60), for which no or limited effects were observed in the tested biological systems upon exposure to PA6-rGO or rGO. At the same time, the *in vivo* results highlight the limitations of single cell type *in vitro* models as alternative models to animals for predictive toxicology and support the current trend to adopt co-culture *in vitro* models to better replicate *in vivo* outcomes. Future studies should therefore investigate the applicability of co-cultures of A549/dTHP-1 cells, lung-on-a-chip, or whole alveoli organoid models for the screening of GRMs.
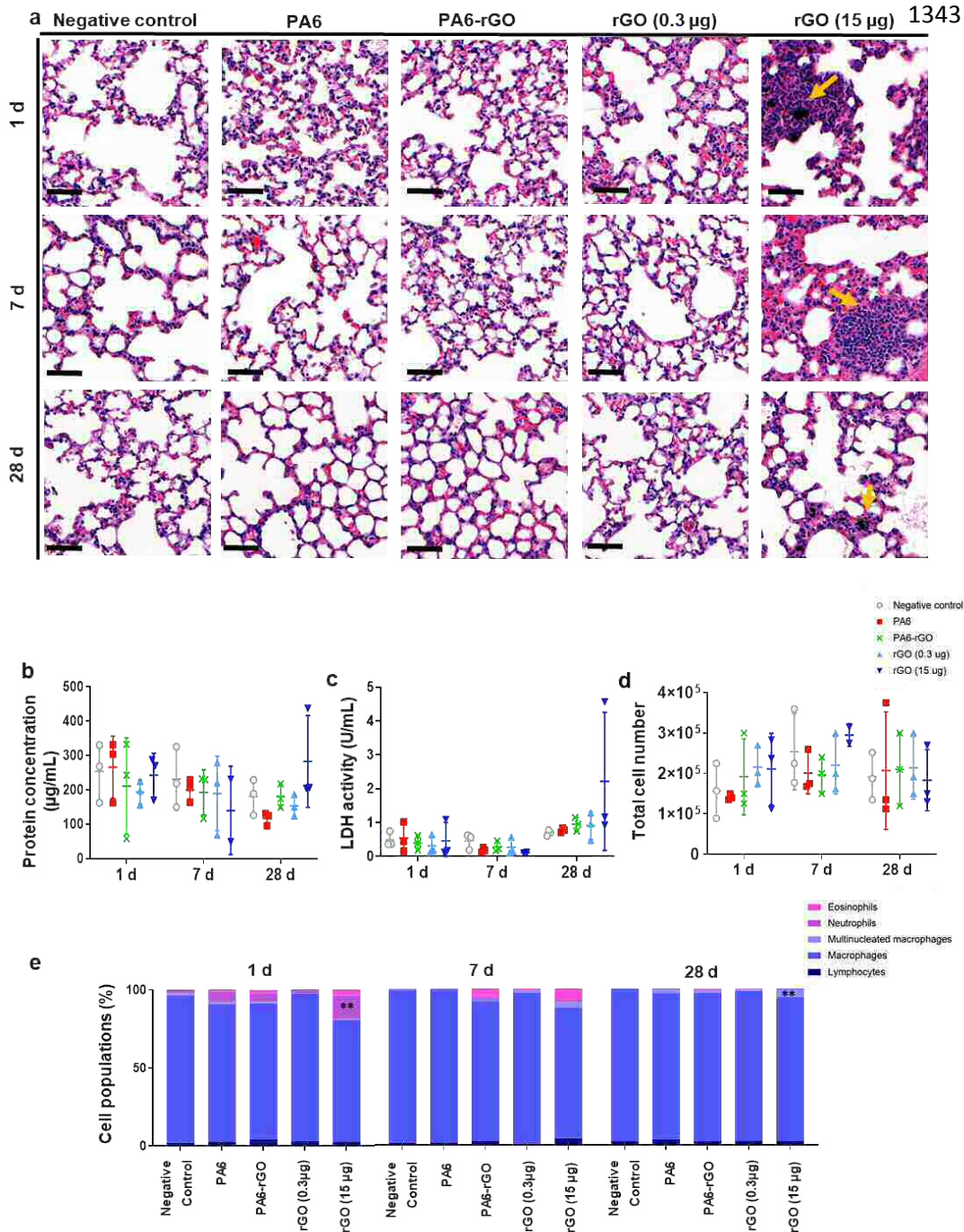
Figure 7. Animals (n= 3) were exposed by oropharyngeal aspiration to abraded polymer (PA6, 15 µg), abraded composite (PA6-rGO, 15 µg; with 2.5% rGO, hence 0.375 µg of rGO in 15 µg of PA6-rGO), reduced graphene oxide (rGO, 0.3 µg or 15 µg; 2.5% of 15 µg equals to about 0.3 µg), or negative control (BSA 0.1% in water). (a) Representative images of H&E-stained lung sections from mice exposed to rGO and abraded composites, following 1, 7 and 28 days after oropharyngeal aspiration. Arrows indicate the formation of granulomas after treatment with rGO. (b) Protein concentration and (c) LDH activity in BAL fluid of exposed mice(d) Total cell number and (e) cell

population (%) of BAL samples from mice after 1, 7 and 28 days following material administration. Data are presented as mean ± SD. The * symbol represents $p < 0.05$ as compared to the negative control.
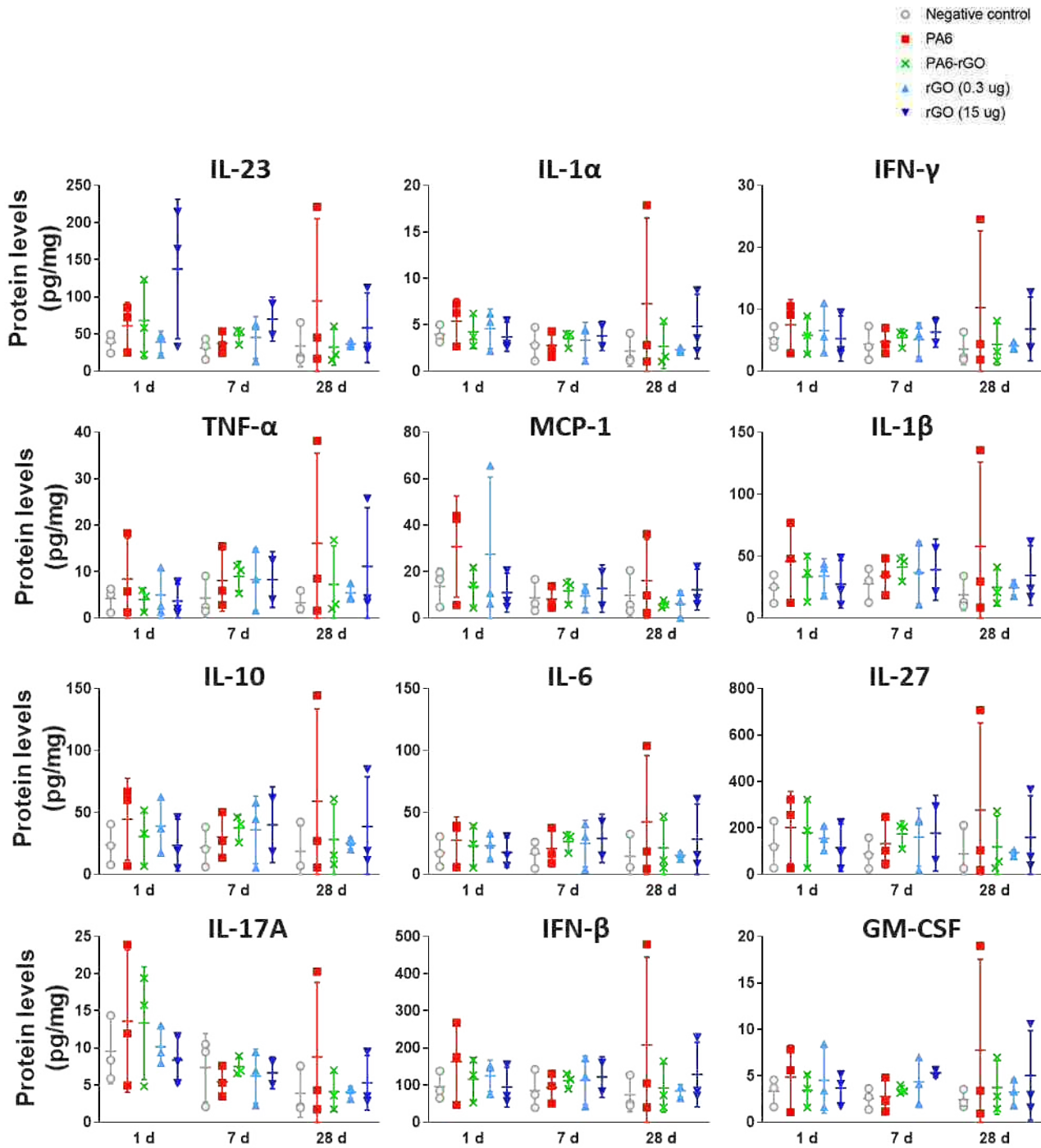
Figure 8. Inflammatory response to rGO and abraded composite materials (neat PA6, PA6-rGO) in the lungs of mice after 1, 7 and 28 days. Individual data points corresponding to each animal are plotted alongside mean values. Data are presented as mean ± SD.

Conclusions

Numerous studies have addressed the hazard potential of GRMs using a variety of model systems.[26] These studies attest to the key importance of defining the properties of the tested materials including the lateral dimensions, thickness, number of layers, and C:O ratio.[27] It is noted that most, if not all of these studies have been carried out using pristine (as-produced) materials. However, this may not accurately reflect the actual handling and use of GRMs during their life cycle as components of GRM-enabled products.[141] In a previous study conducted using multi-walled carbon nanotubes (MWCNTs), the as-produced MWCNTs were shown to elicit inflammation when administered to mice *via* pharyngeal aspiration whereas the aerosols generated from sanding of composites containing polymer-coated MWCNTs, representative of the actual end-product, did not exert such toxicity.[142] Herein, we applied similar product life cycle considerations to assess the toxicological impact of rGO in the context of its embedding in a thermoplastic PA6 polymer matrix and its potential release during the life cycle of rGO-reinforced PA6 composites. A multi-endpoint comparison was performed between as-produced rGO, abraded PA6-rGO composite and abraded neat PA6 using a panel of robust and commonly used *in vitro* models as well as a mouse model of pulmonary exposure. Overall, the present findings show a negligible impact of rGO-reinforced PA6 composites on all the models tested, suggesting a likely low risk to human health at acute exposure conditions. Nevertheless, the results found for rGO alone, in particular *in vivo*, suggest that long-term effects after repeated exposure cannot be excluded and further studies are required to address the possible chronic impact of rGO-reinforced composite materials.

Declaration of interests

The authors declare that they have no known competing financial interests or personal relationships that could have appeared to influence the work reported in this paper.

Supporting Information

The Supporting Information is available free of charge.

Raman spectra, and FTIR patterns of GO, rGO and functionalised rGO, XPS spectra and TGA analysis of functionalized rGO, representative TEM micrographs of rGO after the APTES functionalization, representative AFM and optical microscopy images of rGO and PA6-rGO, Lateral dimension and thickness distribution analysis for rGO and PA6-rGO, EPR spectra of the powder of PA6, rGO and PA6-rGO and assessment of ROS, particle size distributions of PA6-rGO and PA6 particles measured by SMPS, TNF-α Expression Test (TET) for endotoxin detection in HMDMs exposed to PA6, PA6-rGO, and rGO, representative SEM images of the crack surface of the freeze-fractured samples of neat PA6 and PA6-rGO composite, representative TEM image of the abraded particles from the PA6-rGO composite showing the protruding rGOs from PA6 matrix, IL-6 and IL-8 release after DQ exposure in A549 lung cells, LDH release from RAW 264.7 macrophages after exposure to rGO and abraded PA6 and PA6-rGO for 24 h, IFN-γ, TNF-α and IL-1β release by THP-1 macrophages after incubation with 20 µg/mL of PA6, PA6-rGO and rGO, cell morphology of RAW 264.7 macrophages exposed to different concentrations of rGO and abraded PA6 and PA6-rGO composites, cytokine profiling and hierarchical cluster analysis of inflammatory mediators released in differentiated HL-60 neutrophils exposed to rGO, abraded PA6-rGO and PA6, interference assessment of the abraded particles (PA6 and PA6-rGO) and rGO with the MTS assay.

References

(1)   George, G.; Sisupal, S. B.; Tomy, T.; Kumaran, A.; Vadivelu, P.; Suvekbala, V.; Sivaram, S.; Ragupathy, L. Facile, Environmentally Benign and Scalable Approach to Produce Pristine Few Layers Graphene Suitable for Preparing Biocompatible Polymer Nanocomposites. *Sci. Rep.* **2018**, *8* (1), 11228. https://doi.org/10.1038/s41598-018-28560-

1427   1.

1428   (2)   Novoselov, K. S.; Fal'Ko, V. I.; Colombo, L.; Gellert, P. R.; Schwab, M. G.; Kim, K. A
1429   Roadmap for Graphene. *Nature*. **2012**, 192–200. https://doi.org/10.1038/nature11458.

1430   (3)   Geim, A. K.; Novoselov, K. S. The Rise of Graphene. *Nat. Mater.* **2007**, *6* (3), 183–191.
1431   https://doi.org/10.1038/nmat1849.

1432   (4)   Ferrari, A. C.; Bonaccorso, F.; Fal'ko, V.; Novoselov, K. S.; Roche, S.; Bøggild, P.; Borini,
1433   S.; Koppens, F. H. L.; Palermo, V.; Pugno, N.; Garrido, J. A.; Sordan, R.; Bianco, A.;
1434   Ballerini, L.; Prato, M.; Lidorikis, E.; Kivioja, J.; Marinelli, C.. Science and Technology
1435   Roadmap for Graphene, Related Two-Dimensional Crystals, and Hybrid Systems.
1436   *Nanoscale* **2015**, *7* (11), 4598–4810. https://doi.org/10.1039/C4NR01600A.

1437   (5)   Reiss, T.; Hjelt, K.; Ferrari, A. C. Graphene Is on Track to Deliver on Its Promises. *Nat.*
1438   *Nanotech.* **2019**, 907–910. https://doi.org/10.1038/s41565-019-0557-0.

1439   (6)   Kong, W.; Kum, H.; Bae, S. H.; Shim, J.; Kim, H.; Kong, L.; Meng, Y.; Wang, K.; Kim,
1440   C.; Kim, J. Path towards Graphene Commercialization from Lab to Market. *Nature*
1441   *Nanotechnology*. **2019**, 927–938. https://doi.org/10.1038/s41565-019-0555-2.

1442   (7)   Stankovich, S.; Dikin, D. A.; Dommett, G. H. B.; Kohlhaas, K. M.; Zimney, E. J.; Stach, E.
1443   A.; Piner, R. D.; Nguyen, S. B. T.; Ruoff, R. S. Graphene-Based Composite Materials.
1444   *Nature* **2006**, *442* (7100), 282–286. https://doi.org/10.1038/nature04969.

1445   (8)   Zhao, X.; Zhang, Q.; Chen, D.; Lu, P. Enhanced Mechanical Properties of Graphene-Based
1446   Polyvinyl Alcohol Composites. *Macromolecules* **2010**, *43* (5), 2357–2363.
1447   https://doi.org/10.1021/ma902862u.

1448   (9)   Bortz, D. R.; Heras, E. G.; Martin-Gullon, I. Impressive Fatigue Life and Fracture
1449   Toughness Improvements in Graphene Oxide/Epoxy Composites. *Macromolecules* **2012**,
1450   *45* (1), 238–245. https://doi.org/10.1021/ma201563k.

1451   (10)   Song, P.; Cao, Z.; Cai, Y.; Zhao, L.; Fang, Z.; Fu, S. Fabrication of Exfoliated Graphene-
1452   Based Polypropylene Nanocomposites with Enhanced Mechanical and Thermal Properties.
1453   *Polymer (Guildf).* **2011**, *52* (18), 4001–4010.
1454   https://doi.org/10.1016/j.polymer.2011.06.045.

1455   (11)   Wang, Y.; Yu, J.; Dai, W.; Song, Y.; Wang, D.; Zeng, L.; Jiang, N. Enhanced Thermal and
1456   Electrical Properties of Epoxy Composites Reinforced with Graphene Nanoplatelets.
1457   *Polym. Compos.* **2015**, *36* (3), 556–565. https://doi.org/10.1002/pc.22972.

1458   (12)   Shi, Y.; Yu, B.; Zheng, Y.; Yang, J.; Duan, Z.; Hu, Y. Design of Reduced Graphene Oxide
1459   Decorated with DOPO-Phosphanomidate for Enhanced Fire Safety of Epoxy Resin. *J.*
1460   *Colloid Interface Sci.* **2018**, *521*, 160–171. https://doi.org/10.1016/j.jcis.2018.02.054.

1461   (13)   Gong, L.; Yin, B.; Li, L. P.; Yang, M. B. Nylon-6/Graphene Composites Modified through
1462   Polymeric Modification of Graphene. *Compos. Part B Eng.* **2015**, *73*, 49–56.
1463   https://doi.org/10.1016/j.compositesb.2014.12.009.

1464   (14)   Fu, X.; Yao, C.; Yang, G. Recent Advances in Graphene/Polyamide 6 Composites: A
1465   Review. *RSC Advances*., **2015**, 61688–61702. https://doi.org/10.1039/c5ra09312k.

1466　(15)　Mouhmid, B.; Imad, A.; Benseddiq, N.; Benmedakhène, S.; Maazouz, A. A Study of the
1467　　　　 Mechanical Behaviour of a Glass Fibre Reinforced Polyamide 6,6: Experimental
1468　　　　 Investigation. *Polym. Test.* **2006**, *25* (4), 544–552.
1469　　　　 https://doi.org/10.1016/j.polymertesting.2006.03.008.

1470　(16)　Xu, Z.; Gao, C. *In Situ* Polymerization Approach to Graphene-Reinforced Nylon-6
1471　　　　 Composites. *Macromolecules* **2010**, *43* (16), 6716–6723.
1472　　　　 https://doi.org/10.1021/ma1009337.

1473　(17)　Pant, H. R.; Pant, B.; Park, C. H.; Kim, H. J.; Lee, D. S.; Tijing, L. D.; Hwang, B. S.; Kim,
1474　　　　 H. Y.; Kim, C. S. RGO/Nylon-6 Composite Mat with Unique Structural Features and
1475　　　　 Electrical Properties Obtained from Electrospinning and Hydrothermal Process. *Fibers*
1476　　　　 *Polym.* **2013**, *14* (6), 970–975. https://doi.org/10.1007/s12221-013-0970-1.

1477　(18)　O'Neill, A.; Bakirtzis, D.; Dixon, D. Polyamide 6/Graphene Composites: The Effect of *in*
1478　　　　 *Situ* Polymerisation on the Structure and Properties of Graphene Oxide and Reduced
1479　　　　 Graphene Oxide. *Eur. Polym. J.* **2014**, *59*, 353–362.
1480　　　　 https://doi.org/10.1016/j.eurpolymj.2014.07.038.

1481　(19)　Mittal, S.; Kumar, V.; Dhiman, N.; Chauhan, L. K. S.; Pasricha, R.; Pandey, A. K. Physico-
1482　　　　 Chemical Properties Based Differential Toxicity of Graphene Oxide/Reduced Graphene
1483　　　　 Oxide in Human Lung Cells Mediated through Oxidative Stress. *Sci. Rep.* **2016**, *6* (1), 1–
1484　　　　 16. https://doi.org/10.1038/srep39548.

1485　(20)　Chen, G. Y.; Yang, H. J.; Lu, C. H.; Chao, Y. C.; Hwang, S. M.; Chen, C. L.; Lo, K. W.;
1486　　　　 Sung, L. Y.; Luo, W. Y.; Tuan, H. Y.; Hu, Y. C. Simultaneous Induction of Autophagy and
1487　　　　 Toll-like Receptor Signaling Pathways by Graphene Oxide. *Biomaterials* **2012**, *33* (27),
1488　　　　 6559–6569. https://doi.org/10.1016/j.biomaterials.2012.05.064.

1489　(21)　Li, R.; Guiney, L. M.; Chang, C. H.; Mansukhani, N. D.; Ji, Z.; Wang, X.; Liao, Y. P.; Jiang,
1490　　　　 W.; Sun, B.; Hersam, M. C.; Nel, A. E.; Xia, T. Surface Oxidation of Graphene Oxide
1491　　　　 Determines Membrane Damage, Lipid Peroxidation, and Cytotoxicity in Macrophages in a
1492　　　　 Pulmonary Toxicity Model. *ACS Nano* **2018**, *12* (2), 1390–1402.
1493　　　　 https://doi.org/10.1021/acsnano.7b07737.

1494　(22)　Liu, Y.; Luo, Y.; Wu, J.; Wang, Y.; Yang, X.; Yang, R.; Wang, B.; Yang, J.; Zhang, N.
1495　　　　 Graphene Oxide Can Induce *in Vitro* and *in Vivo* Mutagenesis. *Sci. Rep.* **2013**, *3*.
1496　　　　 https://doi.org/10.1038/srep03469.

1497　(23)　Kucki, M.; Rupper, P.; Sarrieu, C.; Melucci, M.; Treossi, E.; Schwarz, A.; León, V.;
1498　　　　 Kraegeloh, A.; Flahaut, E.; Vázquez, E.; Palermo, V.; Wick, P. Interaction of Graphene-
1499　　　　 Related Materials with Human Intestinal Cells: An *in Vitro* Approach. *Nanoscale* **2016**, *8*
1500　　　　 (16), 8749–8760. https://doi.org/10.1039/c6nr00319b.

1501　(24)　Kucki, M.; Aengenheister, L.; Diener, L.; Rippl, A. V.; Vranic, S.; Newman, L.; Vazquez,
1502　　　　 E.; Kostarelos, K.; Wick, P.; Buerki-Thurnherr, T. Impact of Graphene Oxide on Human
1503　　　　 Placental Trophoblast Viability, Functionality and Barrier Integrity. *2D Mater.* **2018**, *5* (3),
1504　　　　 035014. https://doi.org/10.1088/2053-1583/aab9e2.

1505　(25)　Drasler, B.; Kucki, M.; Delhaes, F.; Buerki-Thurnherr, T.; Vanhecke, D.; Korejwo, D.;
1506　　　　 Chortarea, S.; Barosova, H.; Hirsch, C.; Petri-Fink, A.; Rothen-Rutishauser, B.; Wick, P.

Single Exposure to Aerosolized Graphene Oxide and Graphene Nanoplatelets Did Not Initiate an Acute Biological Response in a 3D Human Lung Model. *Carbon N. Y.* **2018**, *137*, 125–135. https://doi.org/10.1016/J.CARBON.2018.05.012.

(26) Fadeel, B.; Bussy, C.; Merino, S.; Vázquez, E.; Flahaut, E.; Mouchet, F.; Evariste, L.; Gauthier, L.; Koivisto, A. J.; Vogel, U.; Martín, C.; Delogu, L. G.; Buerki-Thurnherr, T.; Wick, P.; Beloin-Saint-Pierre, D.; Hischier, R.; Pelin, M.; Candotto Carniel, F.; Tretiach, M.; Cesca, F.. Safety Assessment of Graphene-Based Materials: Focus on Human Health and the Environment. *ACS Nano.* **2018**, 10582–10620. https://doi.org/10.1021/acsnano.8b04758.

(27) Wick, P.; Louw-Gaume, A. E.; Kucki, M.; Krug, H. F.; Kostarelos, K.; Fadeel, B.; Dawson, K. A.; Salvati, A.; Vázquez, E.; Ballerini, L.; Tretiach, M.; Benfenati, F.; Flahaut, E.; Gauthier, L.; Prato, M.; Bianco, A. Classification Framework for Graphene-Based Materials. *Angew. Chemie Int. Ed.* **2014**, *53* (30), 7714–7718. https://doi.org/10.1002/anie.201403335.

(28) Ou, L.; Song, B.; Liang, H.; Liu, J.; Feng, X.; Deng, B.; Sun, T.; Shao, L. Toxicity of Graphene-Family Nanoparticles: A General Review of the Origins and Mechanisms. *Part Fibre Toxicol*. **2016**, 1–24. https://doi.org/10.1186/s12989-016-0168-y.

(29) Froggett, S. J.; Clancy, S. F.; Boverhof, D. R.; Canady, R. A. A Review and Perspective of Existing Research on the Release of Nanomaterials from Solid Nanocomposites. *Part Fibre Toxicol*. **2014**, 1–28. https://doi.org/10.1186/1743-8977-11-17.

(30) Duncan, T. V.; Pillai, K. Release of Engineered Nanomaterials from Polymer Nanocomposites: Diffusion, Dissolution, and Desorption. *ACS Applied Materials and Interfaces*., **2015**, 2–19. https://doi.org/10.1021/am5062745.

(31) Zepp, R.; Ruggiero, E.; Acrey, B.; Acrey, B.; Davis, M. J. B.; Davis, M. J. B.; Han, C.; Han, C.; Han, C.; Hsieh, H. S.; Hsieh, H. S.; Vilsmeier, K.; Wohlleben, W.; Sahle-Demessie, E. Fragmentation of Polymer Nanocomposites: Modulation by Dry and Wet Weathering, Fractionation, and Nanomaterial Filler. *Environ. Sci. Nano* **2020**, *7* (6), 1742–1758. https://doi.org/10.1039/c9en01360a.

(32) Lankone, R. S.; Ruggiero, E.; Goodwin, D. G.; Vilsmeier, K.; Mueller, P.; Pulbere, S.; Challis, K.; Bi, Y.; Westerhoff, P.; Ranville, J.; Fairbrother, D. H.; Sung, L.-P.; Wohlleben, W. Evaluating Performance, Degradation, and Release Behavior of a Nanoform Pigmented Coating after Natural and Accelerated Weathering. *NanoImpact* **2020**, *17*.

(33) Waquier, L.; Myles, B. S.; Henrard, L.; Vautard, F.; Pappas, C. M.; Feneon, B.; Delaitre, C.; Mehlem, J. J.; Khripin, C. Y. Quantitative Measurement of Nanoparticle Release from Rubber Composites during Fabrication and Testing. *J. Nanoparticle Res.* **2020**, *22* (9), 1–10. https://doi.org/10.1007/S11051-020-04977-6/FIGURES/5.

(34) Oberdörster, G.; Oberdörster, E.; Oberdörster, J. Nanotoxicology: An Emerging Discipline Evolving from Studies of Ultrafine Particles. *Environ. Health Perspect.* **2005**, *113* (7), 823–839. https://doi.org/10.1289/ehp.7339.

(35) Pelin, M.; Sosa, S.; Prato, M.; Tubaro, A. Occupational Exposure to Graphene Based Nanomaterials: Risk Assessment. *Nanoscale*. **2018**, 15894–15903.

1548   https://doi.org/10.1039/c8nr04950e.

(36)   Carosio, F.; Maddalena, L.; Gomez, J.; Saracco, G.; Fina, A. Graphene Oxide Exoskeleton to Produce Self Extinguishing, Nonignitable, and Flame Resistant Flexible Foams: A Mechanically Tough Alternative to Inorganic Aerogels. *Adv. Mater. Interfaces* **2018**, *5* (23), 1801288. https://doi.org/10.1002/admi.201801288.

(37)   Gómez, J.; Villaro, E.; Navas, A.; Recio, I. Testing the Influence of the Temperature, RH and Filler Type and Content on the Universal Power Law for New Reduced Graphene Oxide TPU Composites. *Mater. Res. Express* **2017**, *4* (10), 105020. https://doi.org/10.1088/2053-1591/aa8e11.

(38)   Eckmann, A.; Felten, A.; Verzhbitskiy, I.; Davey, R.; Casiraghi, C. Raman Study on Defective Graphene: Effect of the Excitation Energy, Type, and Amount of Defects. *Phys. Rev. B - Condens. Matter Mater. Phys.* **2013**, *88* (3), 035426. https://doi.org/10.1103/PhysRevB.88.035426.

(39)   Beams, R.; Gustavo Cançado, L.; Novotny, L. Raman Characterization of Defects and Dopants in Graphene. *Journal of Physics Condensed Matter*. **2015**, p 083002. https://doi.org/10.1088/0953-8984/27/8/083002.

(40)   Wan, Y. J.; Gong, L. X.; Tang, L. C.; Wu, L. Bin; Jiang, J. X. Mechanical Properties of Epoxy Composites Filled with Silane-Functionalized Graphene Oxide. *Compos. Part A Appl. Sci. Manuf.* **2014**, *64*, 79–89. https://doi.org/10.1016/j.compositesa.2014.04.023.

(41)   Guo, F.; Creighton, M.; Chen, Y.; Hurt, R.; Külaots, I. Porous Structures in Stacked, Crumpled and Pillared Graphene-Based 3D Materials. *Carbon N. Y.* **2014**, *66*, 476–484. https://doi.org/10.1016/j.carbon.2013.09.024.

(42)   Ali, G.; Mehmood, A.; Ha, H. Y.; Kim, J.; Chung, K. Y. Reduced Graphene Oxide as a Stable and High-Capacity Cathode Material for Na-Ion Batteries. *Sci. Rep.* **2017**, *7* (2), 1–8. https://doi.org/10.1038/srep40910.

(43)   Golchin, A.; Simmons, G.; Glavatskih, S.; Prakash, B. Tribological Behaviour of Polymeric Materials in Water-Lubricated Contacts. *Proc. Inst. Mech. Eng. Part J J. Eng. Tribol.* **2013**, *227* (8), 811–825. https://doi.org/10.1177/1350650113476441.

(44)   Irfan, A.; Sachse, S.; Njuguna, J.; Pielichowski, K.; Silva, F.; Zhu, H. Assessment of Nanoparticle Release from Polyamide 6- and Polypropylene-Silicon Composites and Cytotoxicity in Human Lung A549 Cells. *J. Inorg. Organomet. Polym. Mater.* **2013**, *23* (4), 861–870. https://doi.org/10.1007/s10904-013-9856-3.

(45)   Ferreiro, V.; Depecker, C.; Laureyns, J.; Coulon, G. Structures and Morphologies of Cast and Plastically Strained Polyamide 6 Films as Evidenced by Confocal Raman Microspectroscopy and Atomic Force Microscopy. *Polymer (Guildf).* **2004**, *45* (17), 6013–6026. https://doi.org/10.1016/j.polymer.2004.06.018.

(46)   Krishnamoorthy, K.; Veerapandian, M.; Mohan, R.; Kim, S. J. Investigation of Raman and Photoluminescence Studies of Reduced Graphene Oxide Sheets. *Appl. Phys. A Mater. Sci. Process.* **2012**, *106* (3), 501–506. https://doi.org/10.1007/s00339-011-6720-6.

(47)   Song, N.; Yang, J.; Ding, P.; Tang, S.; Shi, L. Effect of Polymer Modifier Chain Length on

1588 Thermal Conductive Property of Polyamide 6/Graphene Nanocomposites. *Compos. Part A*
1589 *Appl. Sci. Manuf.* **2015**, *73*, 232–241. https://doi.org/10.1016/j.compositesa.2015.03.018.

1590 (48) Nel, A.; Xia, T.; Mädler, L.; Li, N. Toxic Potential of Materials at the Nanolevel. *Science*
1591 **2006**, *311* (5761), 622–627. https://doi.org/10.1126/science.1114397.

1592 (49) Su, W. C.; Ku, B. K.; Kulkarni, P.; Cheng, Y. S. Deposition of Graphene Nanomaterial
1593 Aerosols in Human Upper Airways. *J. Occup. Environ. Hyg.* **2016**, *13* (1), 48–59.
1594 https://doi.org/10.1080/15459624.2015.1076162.

1595 (50) Schinwald, A.; Murphy, F. A.; Jones, A.; MacNee, W.; Donaldson, K. Graphene-Based
1596 Nanoplatelets: A New Risk to the Respiratory System as a Consequence of Their Unusual
1597 Aerodynamic Properties. *ACS Nano* **2012**, *6* (1), 736–746.
1598 https://doi.org/10.1021/nn204229f.

1599 (51) Netkueakul, W.; Fischer, B.; Walder, C.; Nüesch, F.; Rees, M.; Jovic, M.; Gaan, S.; Jacob,
1600 P.; Wang, J. Effects of Combining Graphene Nanoplatelet and Phosphorous Flame
1601 Retardant as Additives on Mechanical Properties and Flame Retardancy of Epoxy
1602 Nanocomposite. *Polymers (Basel).* **2020**, *12* (10), 2349.
1603 https://doi.org/10.3390/polym12102349.

1604 (52) Zeng, C.; Lu, S.; Xiao, X.; Gao, J.; Pan, L.; He, Z.; Yu, J. Enhanced Thermal and
1605 Mechanical Properties of Epoxy Composites by Mixing Noncovalently Functionalized
1606 Graphene Sheets. *Polym. Bull.* **2015**, *72* (3), 453–472. https://doi.org/10.1007/s00289-014-
1607 1280-5.

1608 (53) Gomez, J.; Villaro, E.; Karagiannidis, P. G.; Elmarakbi, A. Effects of Chemical Structure
1609 and Morphology of Graphene-Related Materials (GRMs) on Melt Processing and Properties
1610 of GRM/Polyamide-6 Nanocomposites. *Results Mater.* **2020**, *7*, 100105.
1611 https://doi.org/10.1016/j.rinma.2020.100105.

1612 (54) Zok, F. W.; Miserez, A. Property Maps for Abrasion Resistance of Materials. *Acta Mater.*
1613 **2007**, *55* (18), 6365–6371. https://doi.org/10.1016/j.actamat.2007.07.042.

1614 (55) Jian, L.; Ning, L.; Yang, S.; Wang, J.; Hua, M. Triboelectrification Electrostatic Potential
1615 of MC Nylon 6 under Point Contact Dry Sliding. *Tribol. Lett.* **2009**, *36* (3), 199–208.
1616 https://doi.org/10.1007/s11249-009-9473-z.

1617 (56) Li, Y.; Boraschi, D. Endotoxin Contamination: A Key Element in the Interpretation of
1618 Nanosafety Studies. *Nanomedicine*. **2016**, 269–287. https://doi.org/10.2217/nnm.15.196.

1619 (57) Mukherjee, S. P.; Lozano, N.; Kucki, M.; Del Rio-Castillo, A. E.; Newman, L.; Vázquez,
1620 E.; Kostarelos, K.; Wick, P.; Fadeel, B. Detection of Endotoxin Contamination of Graphene
1621 Based Materials Using the TNF-α Expression Test and Guidelines for Endotoxin-Free
1622 Graphene Oxide Production. *PLoS One* **2016**, *11* (11), e0166816.
1623 https://doi.org/10.1371/journal.pone.0166816.

1624 (58) Froggett, S. J.; Clancy, S. F.; Boverhof, D. R.; Canady, R. A. A Review and Perspective of
1625 Existing Research on the Release of Nanomaterials from Solid Nanocomposites. *Particle*
1626 *and Fibre Toxicology*. BioMed Central Ltd. April 7, 2014, pp 1–28.
1627 https://doi.org/10.1186/1743-8977-11-17.

(59) Massaq, A.; Rusinek, A.; Klosak, M.; Bahi, S.; Arias, A. Strain Rate Effect on the Mechanical Behavior of Polyamide Composites under Compression Loading. *Compos. Struct.* **2019**, *214*, 114–122. https://doi.org/10.1016/j.compstruct.2019.01.101.

(60) Zaman, I.; Kuan, H. C.; Dai, J.; Kawashima, N.; Michelmore, A.; Sovi, A.; Dong, S.; Luong, L.; Ma, J. From Carbon Nanotubes and Silicate Layers to Graphene Platelets for Polymer Nanocomposites. *Nanoscale* **2012**, *4* (15), 4578–4586. https://doi.org/10.1039/c2nr30837a.

(61) Zheng, W.; Chen, W. G.; zhao, Q.; Ren, S. X.; Fu, Y. Q. Interfacial Structures and Mechanisms for Strengthening and Enhanced Conductivity of Graphene/Epoxy Nanocomposites. *Polymer (Guildf).* **2019**, *163*, 171–177. https://doi.org/10.1016/j.polymer.2018.12.055.

(62) Netkueakul, W.; Korejwo, D.; Hammer, T.; Chortarea, S.; Rupper, P.; Braun, O.; Calame, M.; Rothen-Rutishauser, B.; Buerki-Thurnherr, T.; Wick, P.; Wang, J. Release of Graphene-Related Materials from Epoxy-Based Composites: Characterization, Quantification and Hazard Assessment: *in Vitro. Nanoscale* **2020**, *12* (19), 10703–10722. https://doi.org/10.1039/c9nr10245k.

(63) Oberdörster, G.; Stone, V.; Donaldson, K. Toxicology of Nanoparticles: A Historical Perspective. *Nanotoxicology* **2009**.

(64) Li, B.; Yang, J.; Huang, Q.; Zhang, Y.; Peng, C.; Zhang, Y.; He, Y.; Shi, J.; Li, W.; Hu, J.; Fan, C. Biodistribution and Pulmonary Toxicity of Intratracheally Instilled Graphene Oxide in Mice. *NPG Asia Mater.* **2013**, *5* (4), e44–e44. https://doi.org/10.1038/am.2013.7.

(65) Mercer, R. R.; Scabilloni, J. F.; Hubbs, A. F.; Wang, L.; Battelli, L. A.; McKinney, W.; Castranova, V.; Porter, D. W. Extrapulmonary Transport of MWCNT Following Inhalation Exposure. *Part. Fibre Toxicol.* **2013**, *10* (1), 38. https://doi.org/10.1186/1743-8977-10-38.

(66) Rodrigues, A. F.; Newman, L.; Jasim, D.; Mukherjee, S. P.; Wang, J.; Vacchi, I. A.; Ménard Moyon, C.; Bianco, A.; Fadeel, B.; Kostarelos, K.; Bussy, C. Size Dependent Pulmonary Impact of Thin Graphene Oxide Sheets in Mice: Toward Safe by Design. *Adv. Sci.* **2020**, *7* (12), 1903200. https://doi.org/10.1002/advs.201903200.

(67) Wu, J.; Wang, Y.; Liu, G.; Jia, Y.; Yang, J.; Shi, J.; Dong, J.; Wei, J.; Liu, X. Characterization of Air-Liquid Interface Culture of A549 Alveolar Epithelial Cells. *Brazilian J. Med. Biol. Res.* **2018**, *51* (2). https://doi.org/10.1590/1414-431x20176950.

(68) Chortarea, S.; Zerimariam, F.; Barosova, H.; Septiadi, D.; Clift, M. J. D.; Petri-Fink, A.; Rothen-Rutishauser, B. Profibrotic Activity of Multiwalled Carbon Nanotubes Upon Prolonged Exposures in Different Human Lung Cell Types. *Appl. Vitr. Toxicol.* **2019**, *5* (1), 47–61. https://doi.org/10.1089/aivt.2017.0033.

(69) Blank, F.; Rothen-Rutishauser, B. M.; Schurch, S.; Gehr, P. An Optimized *in Vitro* Model of the Respiratory Tract Wall to Study Particle Cell Interactions. *J. Aerosol Med.* **2006**, *19* (3), 392–405. https://doi.org/10.1089/jam.2006.19.392.

(70) Chortarea, S.; Clift, M. J. D.; Vanhecke, D.; Endes, C.; Wick, P.; Petri-Fink, A.; Rothen-Rutishauser, B. Repeated Exposure to Carbon Nanotube-Based Aerosols Does Not Affect the Functional Properties of a 3D Human Epithelial Airway Model. *Nanotoxicology* **2015**,

1668   *5390*, 1–11.

(71)   Barosova, H.; Chortarea, S.; Peikertova, P.; Clift, M. J. D.; Petri-Fink, A.; Kukutschova, J.; Rothen-Rutishauser, B. Biological Response of an in Vitro Human 3D Lung Cell Model Exposed to Brake Wear Debris Varies Based on Brake Pad Formulation. *Arch. Toxicol.* **2018**, *92* (7), 2339–2351. https://doi.org/10.1007/s00204-018-2218-8.

(72)   Endes, C.; Schmid, O.; Kinnear, C.; Mueller, S.; Camarero-Espinosa, S.; Vanhecke, D.; Foster, E. J.; Petri-Fink, A.; Rothen-Rutishauser, B.; Weder, C.; Clift, M. J. An *in Vitro* Testing Strategy towards Mimicking the Inhalation of High Aspect Ratio Nanoparticles. *Part. Fibre Toxicol.* **2014**, *11* (1), 40. https://doi.org/10.1186/s12989-014-0040-x.

(73)   Gangwal, S.; Brown, J. S.; Wang, A.; Houck, K. A.; Dix, D. J.; Kavlock, R. J.; Cohen Hubal, E. A. Informing Selection of Nanomaterial Concentrations for ToxCast *in Vitro* Testing Based on Occupational Exposure Potential. *Environmental Health Perspectives*. Environ Health Perspect November 2011, pp 1539–1546. https://doi.org/10.1289/ehp.1103750.

(74)   Chortarea, S.; Barosova, H.; Clift, M. J. D.; Wick, P.; Petri-Fink, A.; Rothen-Rutishauser, B. Human Asthmatic Bronchial Cells Are More Susceptible to Subchronic Repeated Exposures of Aerosolized Carbon Nanotubes At Occupationally Relevant Doses Than Healthy Cells. *ACS Nano* **2017**, *11* (8), 7615–7625. https://doi.org/10.1021/acsnano.7b01992.

(75)   Schlagenhauf, L.; Buerki-Thurnherr, T.; Kuo, Y. Y.; Wichser, A.; Nüesch, F.; Wick, P.; Wang, J. Carbon Nanotubes Released from an Epoxy-Based Nanocomposite: Quantification and Particle Toxicity. *Environ. Sci. Technol.* **2015**, *49* (17), 10616–10623. https://doi.org/10.1021/acs.est.5b02750.

(76)   Mukaida, N. Pathophysiological Roles of Interleukin-8/CXCL8 in Pulmonary Diseases. *American Journal of Physiology - Lung Cellular and Molecular Physiology*. **2003**. https://doi.org/10.1152/ajplung.00233.2002.

(77)   Rincon, M.; Irvin, C. G. Role of IL-6 in Asthma and Other Inflammatory Pulmonary Diseases. *Intern. J. Biol. Sci*. **2012**, 1281–1290. https://doi.org/10.7150/ijbs.4874.

(78)   Wohlleben, W.; Meier, M. W.; Vogel, S.; Landsiedel, R.; Cox, G.; Hirth, S.; Tomović, Ž. Elastic CNT-Polyurethane Nanocomposite: Synthesis, Performance and Assessment of Fragments Released during Use. *Nanoscale* **2013**, *5* (1), 369–380. https://doi.org/10.1039/c2nr32711b.

(79)   Wilbourn, J. D.; McGregor, D. B.; Partensky, C.; Rice, J. M. IARC Reevaluates Silica and Related Substances. *Environ. Health Perspect.* **1997**, *105* (7), 756–759. https://doi.org/10.1289/ehp.97105756.

(80)   Clouter, A.; Brown, D.; Höhr, D.; Borm, P.; Donaldson, K. Inflammatory Effects of Respirable Quartz Collected in Workplaces *versus* Standard DQ12 Quartz: Particle Surface Correlates. *Toxicol. Sci.* **2001**, *63* (1), 90–98.

(81)   Monteiller, C.; Tran, L.; MacNee, W.; Faux, S.; Jones, A.; Miller, B.; Donaldson, K. The Pro-Inflammatory Effects of Low-Toxicity Low-Solubility Particles, Nanoparticles and Fine Particles, on Epithelial Cells *in Vitro*: The Role of Surface Area. *Occup. Environ. Med.*

1708   **2007**, *64* (9), 609–615. https://doi.org/10.1136/oem.2005.024802.

1709 (82) Barosova, H.; Maione, A. G.; Septiadi, D.; Sharma, M.; Haeni, L.; Balog, S.; O'Connell,
1710   O.; Jackson, G. R.; Brown, D.; Clippinger, A. J.; Hayden, P.; Petri-Fink, A.; Stone, V.;
1711   Rothen-Rutishauser, B. Use of EpiAlveolar Lung Model to Predict Fibrotic Potential of
1712   Multiwalled Carbon Nanotubes. *ACS Nano* **2020**, *14* (4), 3941–3956.
1713   https://doi.org/10.1021/acsnano.9b06860.

1714 (83) Nakano-Narusawa, Y.; Yokohira, M.; Yamakawa, K.; Saoo, K.; Imaida, K.; Matsuda, Y.
1715   Single Intratracheal Quartz Instillation Induced Chronic Inflammation and Tumourigenesis
1716   in Rat Lungs. *Sci. Rep.* **2020**, *10* (1), 1–10. https://doi.org/10.1038/s41598-020-63667-4.

1717 (84) Chortarea, S.; Barosova, H.; Clift, M. J. D.; Wick, P.; Petri-Fink, A.; Rothen-Rutishauser,
1718   B. Human Asthmatic Bronchial Cells Are More Susceptible to Subchronic Repeated
1719   Exposures of Aerosolized Carbon Nanotubes at Occupationally Relevant Doses Than
1720   Healthy Cells. *ACS Nano* **2017**, *11* (8), 7615–7625.
1721   https://doi.org/10.1021/acsnano.7b01992.

1722 (85) Beyeler, S.; Chortarea, S.; Rothen-Rutishauser, B.; Petri-Fink, A.; Wick, P.; Tschanz, S. A.;
1723   von Garnier, C.; Blank, F. Acute Effects of Multi-Walled Carbon Nanotubes on Primary
1724   Bronchial Epithelial Cells from COPD Patients. *Nanotoxicology* **2018**, *12* (7), 699–711.
1725   https://doi.org/10.1080/17435390.2018.1472310.

1726 (86) Endes, C.; Schmid, O.; Kinnear, C.; Mueller, S.; Camarero-Espinosa, S.; Vanhecke, D.;
1727   Foster, E. J.; Petri-Fink, A.; Rothen-Rutishauser, B.; Weder, C.; Clift, M. J. D. An *in Vitro*
1728   Testing Strategy towards Mimicking the Inhalation of High Aspect Ratio Nanoparticles.
1729   *Part. Fibre Toxicol.* **2014**, *11* (1). https://doi.org/10.1186/s12989-014-0040-x.

1730 (87) Reshma, S. C.; Syama, S.; Mohanan, P. V. Nano-Biointeractions of PEGylated and Bare
1731   Reduced Graphene Oxide on Lung Alveolar Epithelial Cells: A Comparative *in Vitro* Study.
1732   *Colloids Surfaces B Biointerfaces* **2016**, *140*, 104–116.
1733   https://doi.org/10.1016/j.colsurfb.2015.12.030.

1734 (88) Sohal, I. S.; O'Fallon, K. S.; Gaines, P.; Demokritou, P.; Bello, D. Ingested Engineered
1735   Nanomaterials: State of Science in Nanotoxicity Testing and Future Research Needs. *Part.*
1736   *Fibre Toxicol..*, **2018**, 1–31. https://doi.org/10.1186/s12989-018-0265-1.

1737 (89) Pietroiusti, A.; Bergamaschi, E.; Campagna, M.; Campagnolo, L.; De Palma, G.; Iavicoli,
1738   S.; Leso, V.; Magrini, A.; Miragoli, M.; Pedata, P.; Palombi, L.; Iavicoli, I. The
1739   Unrecognized Occupational Relevance of the Interaction between Engineered
1740   Nanomaterials and the Gastro-Intestinal Tract: A Consensus Paper from a Multidisciplinary
1741   Working Group. *Part. Fibre Toxicol*. **2017**. https://doi.org/10.1186/s12989-017-0226-0.

1742 (90) Kucki, M.; Diener, L.; Bohmer, N.; Hirsch, C.; Krug, H. F.; Palermo, V.; Wick, P. Uptake
1743   of Label-Free Graphene Oxide by Caco-2 Cells Is Dependent on the Cell Differentiation
1744   Status. *J. Nanobiotechnology* **2017**, *15* (1), 46. https://doi.org/10.1186/s12951-017-0280-7.

1745 (91) Domenech, J.; Hernández, A.; Demir, E.; Marcos, R.; Cortés, C. Interactions of Graphene
1746   Oxide and Graphene Nanoplatelets with the *in Vitro* Caco-2/HT29 Model of Intestinal
1747   Barrier. *Sci. Rep.* **2020**, *10* (1), 1–15. https://doi.org/10.1038/s41598-020-59755-0.

(92) Carr, K. E.; Smyth, S. H.; McCullough, M. T.; Morris, J. F.; Moyes, S. M. Morphological Aspects of Interactions between Microparticles and Mammalian Cells: Intestinal Uptake and Onward Movement. *Progress in Histochemistry and Cytochemistry*. **2012**, 185–252. https://doi.org/10.1016/j.proghi.2011.11.001.

(93) Guarnieri, D.; Sánchez-Moreno, P.; Del Rio Castillo, A. E.; Bonaccorso, F.; Gatto, F.; Bardi, G.; Martín, C.; Vázquez, E.; Catelani, T.; Sabella, S.; Pompa, P. P. Biotransformation and Biological Interaction of Graphene and Graphene Oxide during Simulated Oral Ingestion. *Small* **2018**, *14* (24), 1800227. https://doi.org/10.1002/smll.201800227.

(94) Song, Z. M.; Chen, N.; Liu, J. H.; Tang, H.; Deng, X.; Xi, W. S.; Han, K.; Cao, A.; Liu, Y.; Wang, H. Biological Effect of Food Additive Titanium Dioxide Nanoparticles on Intestine: An *in Vitro* Study. *J. Appl. Toxicol.* **2015**, *35* (10), 1169–1178. https://doi.org/10.1002/jat.3171.

(95) Bitounis, D.; Parviz, D.; Cao, X.; Amadei, C. A.; Vecitis, C. D.; Sunderland, E. M.; Thrall, B. D.; Fang, M.; Strano, M. S.; Demokritou, P. Synthesis and Physicochemical Transformations of Size Sorted Graphene Oxide during Simulated Digestion and Its Toxicological Assessment against an *in Vitro* Model of the Human Intestinal Epithelium. *Small* **2020**, *16* (21), 1907640. https://doi.org/10.1002/smll.201907640.

(96) Hansen, G. H.; Niels-Christiansen, L.-L.; Immerdal, L.; Nystrøm, B. T.; Danielsen, E. M. Intestinal Alkaline Phosphatase: Selective Endocytosis from the Enterocyte Brush Border during Fat Absorption. *Am. J. Physiol. Liver Physiol.* **2007**, *293* (6), G1325–G1332. https://doi.org/10.1152/ajpgi.00379.2007.

(97) Hempt, C.; Hirsch, C.; Hannig, Y.; Rippl, A.; Wick, P.; Buerki-Thurnherr, T. Investigating the Effects of Differently Produced Synthetic Amorphous Silica (E 551) on the Integrity and Functionality of the Human Intestinal Barrier Using an Advanced *in Vitro* Co-Culture Model. *Arch. Toxicol.* **2020**, *1*, 3. https://doi.org/10.1007/s00204-020-02957-2.

(98) Accioly, M. T.; Pacheco, P.; Maya-Monteiro, C. M.; Carrossini, N.; Robbs, B. K.; Oliveira, S. S.; Kaufmann, C.; Morgado-Diaz, J. A.; Bozza, P. T.; Viola, J. P. B. Lipid Bodies Are Reservoirs of Cyclooxygenase-2 and Sites of Prostaglandin-E2 Synthesis in Colon Cancer Cells. *Cancer Res.* **2008**, *68* (6), 1732–1740. https://doi.org/10.1158/0008-5472.CAN-07-1999.

(99) Zhang, Y.; Bai, Y.; Jia, J.; Gao, N.; Li, Y.; Zhang, R.; Jiang, G.; Yan, B. Perturbation of Physiological Systems by Nanoparticles. *Chemical Society Reviews*. Royal Society of Chemistry May 21, 2014, pp 3762–3809. https://doi.org/10.1039/c3cs60338e.

(100) Pelin, M.; Fusco, L.; Martín, C.; Sosa, S.; Frontiñán-Rubio, J.; González-Domínguez, J. M.; Durán-Prado, M.; Vázquez, E.; Prato, M.; Tubaro, A. Graphene and Graphene Oxide Induce ROS Production in Human HaCaT Skin Keratinocytes: The Role of Xanthine Oxidase and NADH Dehydrogenase. *Nanoscale* **2018**, *10* (25), 11820–11830. https://doi.org/10.1039/c8nr02933d.

(101) Hänel, K. H.; Cornelissen, C.; Lüscher, B.; Baron, J. M. Cytokines and the Skin Barrier. *International Journal of Molecular Sciences*. Multidisciplinary Digital Publishing Institute (MDPI) April 2013, pp 6720–6745. https://doi.org/10.3390/ijms14046720.

(102) Pelin, M.; Lin, H.; Gazzi, A.; Sosa, S.; Ponti, C.; Ortega, A.; Zurutuza, A.; Vázquez, E.; Prato, M.; Tubaro, A.; Bianco, A. Partial Reversibility of the Cytotoxic Effect Induced by Graphene-Based Materials in Skin Keratinocytes. *Nanomaterials* **2020**, *10* (8), 1–14. https://doi.org/10.3390/nano10081602.

(103) Frontiñán-Rubio, J.; Victoria Gómez, M.; Martín, C.; González-Domínguez, J. M.; Durán-Prado, M.; Vázquez, E. Differential Effects of Graphene Materials on the Metabolism and Function of Human Skin Cells. *Nanoscale* **2018**, *10* (24), 11604–11615. https://doi.org/10.1039/c8nr00897c.

(104) Pelin, M.; Fusco, L.; León, V.; Martín, C.; Criado, A.; Sosa, S.; Vázquez, E.; Tubaro, A.; Prato, M. Differential Cytotoxic Effects of Graphene and Graphene Oxide on Skin Keratinocytes. *Sci. Rep.* **2017**, *7*. https://doi.org/10.1038/srep40572.

(105) Pelin, M.; Fusco, L.; Martín, C.; Sosa, S.; Frontiñán-Rubio, J.; González-Domínguez, J. M.; Durán-Prado, M.; Vázquez, E.; Prato, M.; Tubaro, A. Graphene and Graphene Oxide Induce ROS Production in Human HaCaT Skin Keratinocytes: The Role of Xanthine Oxidase and NADH Dehydrogenase. *Nanoscale* **2018**, *10* (25), 11820–11830. https://doi.org/10.1039/c8nr02933d.

(106) Chang, Y.; Yang, S. T.; Liu, J. H.; Dong, E.; Wang, Y.; Cao, A.; Liu, Y.; Wang, H. *In Vitro* Toxicity Evaluation of Graphene Oxide on A549 Cells. *Toxicol. Lett.* **2011**, *200* (3), 201–210. https://doi.org/10.1016/j.toxlet.2010.11.016.

(107) Wang, Y.; Wu, S.; Zhao, X.; Su, Z.; Du, L.; Sui, A. In Vitro Toxicity Evaluation of Graphene Oxide on Human RPMI 8226 Cells. In *Bio-Medical Materials and Engineering*; IOS Press, 2014; Vol. 24, pp 2007–2013. https://doi.org/10.3233/BME-141010.

(108) Skehan, P.; Storeng, R.; Scudiero, D.; Monks, A.; Mcmahon, J.; Vistica, D.; Warren, J. T.; Bokesch, H.; Kenney, S.; Boyd, M. R. New Colorimetric Cytotoxicity Assay for Anticancer-Drug Screening. *J. Natl. Cancer Inst.* **1990**, *82* (13), 1107–1112. https://doi.org/10.1093/jnci/82.13.1107.

(109) Dias, F. T. G.; Ingracio, A. R.; Nicoletti, N. F.; Menezes, F. C.; Dall Agnol, L.; Marinowic, D. R.; Soares, R. M. D.; da Costa, J. C.; Falavigna, A.; Bianchi, O. Soybean-Modified Polyamide-6 Mats as a Long-Term Cutaneous Wound Covering. *Mater. Sci. Eng. C* **2019**, *99*, 957–968. https://doi.org/10.1016/j.msec.2019.02.019.

(110) Krysiak, Z. J.; Gawlik, M. Z.; Knapczyk-Korczak, J.; Kaniuk, L.; Stachewicz, U. Hierarchical Composite Meshes of Electrospun PS Microfibers with PA6 Nanofibers for Regenerative Medicine. *Materials (Basel).* **2020**, *13* (8), 1974. https://doi.org/10.3390/MA13081974.

(111) Fusco, L.; Pelin, M.; Mukherjee, S.; Keshavan, S.; Sosa, S.; Martín, C.; González, V.; Vázquez, E.; Prato, M.; Fadeel, B.; Tubaro, A. Keratinocytes Are Capable of Selectively Sensing Low Amounts of Graphene-Based Materials: Implications for Cutaneous Applications. *Carbon N. Y.* **2020**, *159*, 598–610. https://doi.org/10.1016/j.carbon.2019.12.064.

(112) Boraschi, D.; Italiani, P.; Palomba, R.; Decuzzi, P.; Duschl, A.; Fadeel, B.; Moghimi, S. M. Nanoparticles and Innate Immunity: New Perspectives on Host Defence. *Seminars Immun.*

2017, 33–51. https://doi.org/10.1016/j.smim.2017.08.013.

(113) Lin, H.; Song, Z.; Bianco, A. How Macrophages Respond to Two-Dimensional Materials: A Critical Overview Focusing on Toxicity. *J. Environ. Sci. Health*. **2021**, 333–356. https://doi.org/10.1080/03601234.2021.1885262.

(114) Mukherjee, S. P.; Kostarelos, K.; Fadeel, B. Cytokine Profiling of Primary Human Macrophages Exposed to Endotoxin-Free Graphene Oxide: Size-Independent NLRP3 Inflammasome Activation. *Adv. Healthc. Mater.* **2018**, *7* (4), 1700815. https://doi.org/10.1002/adhm.201700815.

(115) Russier, J.; Treossi, E.; Scarsi, A.; Perrozzi, F.; Dumortier, H.; Ottaviano, L.; Meneghetti, M.; Palermo, V.; Bianco, A. Evidencing the Mask Effect of Graphene Oxide: A Comparative Study on Primary Human and Murine Phagocytic Cells. *Nanoscale* **2013**, *5* (22), 11234–11247. https://doi.org/10.1039/c3nr03543c.

(116) Mukherjee, S. P.; Bottini, M.; Fadeel, B. Graphene and the Immune System: A Romance of Many Dimensions. *Fro. Immun.* **2017**, 1. https://doi.org/10.3389/fimmu.2017.00673.

(117) Roberts, J. R.; Mercer, R. R.; Stefaniak, A. B.; Seehra, M. S.; Geddam, U. K.; Chaudhuri, I. S.; Kyrlidis, A.; Kodali, V. K.; Sager, T.; Kenyon, A.; Bilgesu, S. A.; Eye, T.; Scabilloni, J. F.; Leonard, S. S.; Fix, N. R.; Schwegler-Berry, D.; Farris, B. Y.; Wolfarth, M. G.; Porter, D. W.; Castranova, V.. Evaluation of Pulmonary and Systemic Toxicity Following Lung Exposure to Graphite Nanoplates: A Member of the Graphene-Based Nanomaterial Family. *Part. Fibre Toxicol.* **2016**, *13* (1), 1–22. https://doi.org/10.1186/s12989-016-0145-5.

(118) Bengtson, S.; Knudsen, K. B.; Kyjovska, Z. O.; Berthing, T.; Skaug, V.; Levin, M.; Koponen, I. K.; Shivayogimath, A.; Booth, T. J.; Alonso, B.; Pesquera, A.; Zurutuza, A.; Thomsen, B. L.; Troelsen, J. T.; Jacobsen, N. R.; Vogel, U. Differences in Inflammation and Acute Phase Response but Similar Genotoxicity in Mice Following Pulmonary Exposure to Graphene Oxide and Reduced Graphene Oxide. *PLoS One* **2017**, *12* (6), e0178355. https://doi.org/10.1371/journal.pone.0178355.

(119) Wu, Y.; Wang, F.; Wang, S.; Ma, J.; Xu, M.; Gao, M.; Liu, R.; Chen, W.; Liu, S. Reduction of Graphene Oxide Alters Its Cyto-Compatibility towards Primary and Immortalized Macrophages. *Nanoscale* **2018**, *10* (30), 14637–14650. https://doi.org/10.1039/c8nr02798f.

(120) Zhou, H.; Zhao, K.; Li, W.; Yang, N.; Liu, Y.; Chen, C.; Wei, T. The Interactions between Pristine Graphene and Macrophages and the Production of Cytokines/Chemokines *via* TLR- and NF-KB-Related Signaling Pathways. *Biomaterials* **2012**, *33* (29), 6933–6942. https://doi.org/10.1016/j.biomaterials.2012.06.064.

(121) Sun, B.; Wang, X.; Ji, Z.; Li, R.; Xia, T. NLRP3 Inflammasome Activation Induced by Engineered Nanomaterials. *Small*. NIH Public Access May 27, 2013, pp 1595–1607. https://doi.org/10.1002/smll.201201962.

(122) Mukherjee, S. P.; Kostarelos, K.; Fadeel, B. Cytokine Profiling of Primary Human Macrophages Exposed to Endotoxin-Free Graphene Oxide: Size-Independent NLRP3 Inflammasome Activation. *Adv. Healthc. Mater.* **2018**, *7* (4). https://doi.org/10.1002/adhm.201700815.

(123) Ma, J.; Liu, R.; Wang, X.; Liu, Q.; Chen, Y.; Valle, R. P.; Zuo, Y. Y.; Xia, T.; Liu, S. Crucial Role of Lateral Size for Graphene Oxide in Activating Macrophages and Stimulating Pro-Inflammatory Responses in Cells and Animals. *ACS Nano* **2015**, *9* (10), 10498–10515. https://doi.org/10.1021/acsnano.5b04751.

(124) Gurunathan, S.; Kang, M.-H.; Jeyaraj, M.; Kim, J.-H. Differential Immunomodulatory Effect of Graphene Oxide and Vanillin-Functionalized Graphene Oxide Nanoparticles in Human Acute Monocytic Leukemia Cell Line (THP-1). *Int. J. Mol. Sci.* **2019**, *20* (2), 247. https://doi.org/10.3390/ijms20020247.

(125) Farcal, L.; Andón, F. T.; Di Cristo, L.; Rotoli, B. M.; Bussolati, O.; Bergamaschi, E.; Mech, A.; Hartmann, N. B.; Rasmussen, K.; Riego-Sintes, J.; Ponti, J.; Kinsner-Ovaskainen, A.; Rossi, F.; Oomen, A.; Bos, P.; Chen, R.; Bai, R.; Chen, C.; Rocks, L.; Fulton, N.Comprehensive *in Vitro* Toxicity Testing of a Panel of Representative Oxide Nanomaterials: First Steps towards an Intelligent Testing Strategy. *PLoS One* **2015**, *10* (5). https://doi.org/10.1371/journal.pone.0127174.

(126) Wang, X.; Duch, M. C.; Mansukhani, N.; Ji, Z.; Liao, Y.-P.; Wang, M.; Zhang, H.; Sun, B.; Chang, C. H.; Li, R.; Lin, S.; Meng, H.; Xia, T.; Hersam, M. C.; Nel, A. E. Use of a Pro-Fibrogenic Mechanism-Based Predictive Toxicological Approach for Tiered Testing and Decision Analysis of Carbonaceous Nanomaterials. *ACS Nano* **2015**, *9* (3), 3032–3043. https://doi.org/10.1021/nn507243w.

(127) Li, J.; Wang, X.; Mei, K. C.; Chang, C. H.; Jiang, J.; Liu, X.; Liu, Q.; Guiney, L. M.; Hersam, M. C.; Liao, Y. P.; Meng, H.; Xia, T. Lateral Size of Graphene Oxide Determines Differential Cellular Uptake and Cell Death Pathways in Kupffer Cells, LSECs, and Hepatocytes. *Nano Today* **2021**, *37*, 101061. https://doi.org/10.1016/J.NANTOD.2020.101061.

(128) Keshavan, S.; Calligari, P.; Stella, L.; Fusco, L.; Delogu, L. G.; Fadeel, B. Nano-Bio Interactions: A Neutrophil-Centric View. *Cell Death Dis.* **2019**, 1–11. https://doi.org/10.1038/s41419-019-1806-8.

(129) Mukherjee, S. P.; Lazzaretto, B.; Hultenby, K.; Newman, L.; Rodrigues, A. F.; Lozano, N.; Kostarelos, K.; Malmberg, P.; Fadeel, B. Graphene Oxide Elicits Membrane Lipid Changes and Neutrophil Extracellular Trap Formation. *Chem* **2018**, *4* (2), 334–358. https://doi.org/10.1016/j.chempr.2017.12.017.

(130) Mukherjee, S. P.; Gliga, A. R.; Lazzaretto, B.; Brandner, B.; Fielden, M.; Vogt, C.; Newman, L.; Rodrigues, A. F.; Shao, W.; Fournier, P. M.; Toprak, M. S.; Star, A.; Kostarelos, K.; Bhattacharya, K.; Fadeel, B. Graphene Oxide Is Degraded by Neutrophils and the Degradation Products Are Non-Genotoxic. *Nanoscale* **2018**, *10* (3), 1180–1188. https://doi.org/10.1039/c7nr03552g.

(131) Kurapati, R.; Russier, J.; Squillaci, M. A.; Treossi, E.; Ménard-Moyon, C.; Del Rio-Castillo, A. E.; Vazquez, E.; Samorì, P.; Palermo, V.; Bianco, A. Dispersibility-Dependent Biodegradation of Graphene Oxide by Myeloperoxidase. *Small* **2015**, *11* (32), 3985–3994. https://doi.org/10.1002/smll.201500038.

(132) EC, C.; Q, Z.; Y, X. The Effect of Sedimentation and Diffusion on Cellular Uptake of Gold

Nanoparticles. *Nat. Nanotechnol.* **2011**, *6* (6), 385–391. https://doi.org/10.1038/NNANO.2011.58.

(133) CY, W.; GM, D.; A, P.; P, D. Buoyant Nanoparticles: Implications for Nano-Biointeractions in Cellular Studies. *Small* **2016**, *12* (23), 3172–3180. https://doi.org/10.1002/SMLL.201600314.

(134) DeLoid, G.; Cohen, J. M.; Darrah, T.; Derk, R.; Rojanasakul, L.; Pyrgiotakis, G.; Wohlleben, W.; Demokritou, P. Estimating the Effective Density of Engineered Nanomaterials for in Vitro Dosimetry. *Nat. Commun. 2014 51* **2014**, *5* (1), 1–10. https://doi.org/10.1038/ncomms4514.

(135) DeLoid, G. M.; Cohen, J. M.; Pyrgiotakis, G.; Pirela, S. V.; Pal, A.; Liu, J.; Srebric, J.; Demokritou, P. Advanced Computational Modeling for *in Vitro* Nanomaterial Dosimetry. *Part. Fibre Toxicol. 2015 121* **2015**, *12* (1), 1–20. https://doi.org/10.1186/S12989-015-0109-1.

(136) Böhmert, L.; König, L.; Sieg, H.; Lichtenstein, D.; Paul, N.; Braeuning, A.; Voigt, A.; Lampen, A. *In Vitro* Nanoparticle Dosimetry for Adherent Growing Cell Monolayers Covering Bottom and Lateral Walls. *Part. Fibre Toxicol. 2018 151* **2018**, *15* (1), 1–20. https://doi.org/10.1186/S12989-018-0278-9.

(137) Williams, G. T.; Williams, W. J. Granulomatous Inflammation - A Review. *Journal of Clinical Pathology*. BMJ Publishing Group 1983, pp 723–733. https://doi.org/10.1136/jcp.36.7.723.

(138) Anderson, J. M.; Rodriguez, A.; Chang, D. T. Foreign Body Reaction to Biomaterials. *Sem. Immun*. **2008**, 86–100. https://doi.org/10.1016/j.smim.2007.11.004.

(139) Poulsen, S. S.; Bengtson, S.; Williams, A.; Jacobsen, N. R.; Troelsen, J. T.; Halappanavar, S.; Vogel, U. A Transcriptomic Overview of Lung and Liver Changes One Day after Pulmonary Exposure to Graphene and Graphene Oxide. *Toxicol. Appl. Pharmacol.* **2021**, *410*, 115343. https://doi.org/10.1016/j.taap.2020.115343.

(140) Moalli, P. A.; MacDonald, J. L.; Goodglick, L. A.; Kane, A. B. Acute Injury and Regeneration of the Mesothelium in Response to Asbestos Fibers. *Am. J. Pathol.* **1987**, *128* (3), 426–445.

(141) Guinée, J. B.; Heijungs, R.; Vijver, M. G.; Peijnenburg, W. J. G. M. Setting the Stage for Debating the Roles of Risk Assessment and Life-Cycle Assessment of Engineered Nanomaterials. *Nat. Nanotech*. **2017**, 727–733. https://doi.org/10.1038/NNANO.2017.135.

(142) Bishop, L.; Cena, L.; Orandle, M.; Yanamala, N.; Dahm, M. M.; Eileen Birch, M.; Evans, D. E.; Kodali, V. K.; Eye, T.; Battelli, L.; Zeidler-Erdely, P. C.; Casuccio, G.; Bunker, K.; Lupoi, J. S.; Lersch, T. L.; Stefaniak, A. B.; Sager, T.; Afshari, A.; Schwegler-Berry, D.; Friend, S.;. *In Vivo* Toxicity Assessment of Occupational Components of the Carbon Nanotube Life Cycle to Provide Context to Potential Health Effects. *ACS Nano* **2017**, *11* (9), 8849–8863. https://doi.org/10.1021/acsnano.7b03038.

(143) Fadeel, B.; Åhlin, A.; Henter, J. I.; Orrenius, S.; Hampton, M. B. Involvement of Caspases in Neutrophil Apoptosis: Regulation by Reactive Oxygen Species. *Blood* **1998**, *92* (12),

4808–4818. https://doi.org/10.1182/blood.v92.12.4808.424k01_4808_4818.

(144) Bhattacharya, K.; Kiliç, G.; Costa, P. M.; Fadeel, B. Cytotoxicity Screening and Cytokine Profiling of Nineteen Nanomaterials Enables Hazard Ranking and Grouping Based on Inflammogenic Potential. *Nanotoxicology* **2017**, *11* (6), 809–826. https://doi.org/10.1080/17435390.2017.1363309.

(145) Khandagale, A.; Lazzaretto, B.; Carlsson, G.; Sundin, M.; Shafeeq, S.; Römling, U.; Fadeel, B. JAGN1 Is Required for Fungal Killing in Neutrophil Extracellular Traps: Implications for Severe Congenital Neutropenia. *J. Leukoc. Biol.* **2018**, No. July, 1–15. https://doi.org/10.1002/JLB.4A0118-030RR.

(146) Elliott, J. T.; Rösslein, M.; Song, N. W.; Toman, B.; Kinsner-Ovaskainen, A.; Maniratanachote, R.; Salit, M. L.; Petersen, E. J.; Sequeira, F.; Romsos, E. L.; Kim, S. J.; Lee, J.; Von Moos, N. R.; Rossi, F.; Hirsch, C.; Krug, H. F.; Suchaoin, W.; Wick, P. Toward Achieving Harmonization in a Nanocytotoxicity Assay Measurement through an Interlaboratory Comparison Study. *ALTEX* **2017**, *34* (2), 201–218. https://doi.org/10.14573/altex.1605021.

Click here to access/download
Supplementary Material
20220902_ Chortarea et al_final version_SI revised
final.docx

Credit author statement

Savvina Chortarea: writing – original draft, investigation, formal analysis, data curation

Ogul Can Kuru: investigation

Woranan Netkueakul: methodology, investigation

Marco Pelin: writing – review & editing, methodology, data curation, investigation, validation, formal analysis, data curation

Sandeep Keshavan: methodology, investigation, formal analysis, data curation

Zhengmei Song: methodology, investigation

Baojin Ma: methodology, investigation

Julio Gómes: data curation, investigation

Elvira Villaro Abalos: data curation, investigation

Luis Augusto Visani de Luna: methodology, investigation

Thomas Loret: investigation

Alexander Fordham: investigation

Matthew Drummond: investigation

Nikolaos Kontis: methodology, investigation

George Anagnostopoulos: methodology, investigation

George Paterakis: methodology, investigation

Pietro Cataldi: investigation

Aurelia Tubaro: investigation

Costas Galiotis: conceptualization, supervision, writing – review & editing, resources, data curation, funding acquisition

Ian Kinloch: data curation, supervision, writing – review & editing,

Bengt Fadeel: conceptualization, supervision, writing – review & editing, validation, resources, project administration, data curation, funding acquisition

Cyrill Bussy: supervision, writing – review & editing, validation, project administration,

Kostas Kostarelos: supervision, writing – review & editing, resources, data curation, funding acquisition

Tina Buerki-Thurnherr: conceptualization, visualization, supervision, validation, writing – review & editing, data curation

Maurizio Prato: conceptualization, supervision, writing – review & editing, resources, project administration, funding acquisition

Alberto Bianco: conceptualization, supervision, writing – review & editing, resources, project administration, funding acquisition

Declaration of interests

☒The authors declare that they have no known competing financial interests or personal relationships that could have appeared to influence the work reported in this paper.

☐The authors declare the following financial interests/personal relationships which may be considered as potential competing interests: